Deep-Sea Research II ■ (■■■■) ■■■–■■■

Contents lists available at SciVerse ScienceDirect

Deep-Sea Research II

journal homepage: www.elsevier.com/locate/dsr2

A multivariate analysis of observed and modeled biophysical variability on the Bering Sea shelf: Multidecadal hindcasts (1970–2009) and forecasts (2010–2040)

Albert J. Hermann [a,*], Georgina A. Gibson [b], Nicholas A. Bond [a], Enrique N. Curchitser [c], Kate Hedstrom [d], Wei Cheng [a], Muyin Wang [a], Phyllis J. Stabeno [e], Lisa Eisner [f], Kristin D. Cieciel [f]

[a] Joint Institute for the Study of the Atmosphere and Ocean, University of Washington, Seattle, WA 98195, USA
[b] International Arctic Research Center, University of Alaska Fairbanks, Fairbanks, AK 99775, USA
[c] Institute of Marine and Coastal Sciences, Rutgers University, New Brunswick, NJ 08901, USA
[d] Arctic Region Supercomputing Center, Fairbanks, AK 99775, USA
[e] Ocean Environment Research Division, NOAA/PMEL, Seattle, WA 98195, USA
[f] Auke Bay Laboratories, NOAA, Juneau, AK 99801, USA

ARTICLE INFO

Keywords:
USA
Alaska
Bering Sea
Modeling

ABSTRACT

Coupled physical/biological models can be used to downscale global climate change to the ecology of subarctic regions, and to explore the bottom-up and top-down effects of that change on the spatial structure of subarctic ecosystems—for example, the relative dominance of large vs. small zooplankton in relation to ice cover. Here we utilize a multivariate statistical approach to extract the emergent properties of a coupled physical/biological hindcast of the Bering Sea for years 1970–2009, which includes multiple episodes of warming and cooling (e.g. the recent cooling of 2005–2009), and a multidecadal regional forecast of the coupled models, driven by an IPCC global model forecast of 2010–2040. Specifically, we employ multivariate empirical orthogonal function (EOF) analysis to derive the spatial covariance among physical and biological timeseries from our simulations. These are compared with EOFs derived from spatially gridded measurements of the region, collected during multiyear field programs. The model replicates observed relationships among temperature and salinity, as well as the observed inverse correlation between temperature and large crustacean zooplankton on the southeastern Bering Sea shelf. Predicted future warming of the shelf is accompanied by a northward shift in both pelagic and benthic biomass.

1. Introduction

1.1. The Bering Sea ecosystem

The hydrography and climatology of the Bering Sea result in a highly productive ecosystem, with huge populations of plankton, shellfish, finfish, marine birds and marine mammals. This ecosystem supports major fisheries. Such intense production derives in part from a broad shelf with strong tides, plentiful iron, and seasonal stratification, adjacent to a deep, macronutrient-rich basin. The southeastern shelf includes three biophysical domains: a well-mixed inner region (~0–50 m), a middle region which is well-mixed in the winter and has two distinct layers in the summer (~50–100 m), and an outer region which is more gradually stratified (~100–200 m) (Coachman, 1986; Kachel et al., 2002). Within these regimes, the relative magnitude of pelagic vs. benthic pathways of carbon flux varies interannually, and is believed to be strongly influenced by the extent of seasonal ice through its effects on stratification (Hunt et al., 2002). Recent cooling trends in the Bering Sea (Stabeno et al., 2012a) have been documented by the Bering Sea Ecosystem Program (BEST), the Bering Sea Integrated Ecosystem Research Program (BSIERP), the US Bering-Aleutian Salmon International Survey (BASIS), and the North Pacific Climate Regimes and Ecosystem Productivity Program (NPCREP). The relative importance of pelagic vs. benthic pathways is likely to shift under the influence of global warming, partially through its impact on seasonal ice extent in the Bering Sea. Field data suggest that recent cold temperatures in the Bering Sea have led to an increase in large crustacean zooplankton, favored as food items by juvenile pollock in the fall season (Coyle et al., 2011).

The revised "oscillating control hypothesis" (OCH) of Hunt et al. (2011) relates temperature and seasonal ice cover in the

* Corresponding author at: Pacific Marine Environmental Laboratory, 7600 Sand Point Way NE, Seattle, WA 98115 USA. . Tel.: +1 206 526 6495; fax: +1 206 526 6485.
E-mail address: albert.j.hermann@noaa.gov (A.J. Hermann).

0967-0645/$ - see front matter © 2013 Elsevier Ltd. All rights reserved.
http://dx.doi.org/10.1016/j.dsr2.2013.04.007

southeastern Bering Sea to the production of zooplankton and fish. This revised hypothesis may be summarized as follows.

Under warm conditions, the seasonal ice cover melts early in the year (February–March). This releases freshwater at the surface, but there is too much mixing and not enough sunlight to support a phytoplankton bloom at this time. Instead, the bloom occurs later (May–June), due to thermal stratification of relatively warm waters. These conditions favor the growth of small neritic copepods, as compared to large crustacean zooplankton (LCZ) (mid- to large-sized copepods, e.g. *Calanus marhallae*, and euphausiids, e.g. *Thysanoessa rashii* and *Thysanoessa inermis*). In general, these warm conditions promote energy flow into the pelagic (vs. benthic) food chain.

Under cold conditions, the ice cover melts late in the year (March–April), and an early bloom (April–May) follows due to the enhanced stratification of the water column. These conditions do not necessarily impede the growth of small neritic copepods, but do enhance the production of larger copepods, which need the early bloom to recruit from nauplii to copepodites in the southeastern Bering Sea. Less of this spring production goes into the pelagic food chain, and more into the benthic food chain.

The OCH also includes the linkage of these lower trophic dynamics to fish recruitment. These will not be considered in this paper, since our model includes only physics through zooplankton. Future research with a model including fish (Aydin et al., unpublished) will address these issues.

1.2. The multivariate analysis

Coupled physical/biological models can be used to downscale global climate change to the ecology of subarctic regions, and to explore the bottom-up and top-down effects of that change on the spatial structure of subarctic ecosystems, such as those predicted by the OCH. If an ice-free Bering is fundamentally different from one with ice cover, we can expect biophysical "modes" to emerge in a statistical analysis of models and data. Other atmospheric factors, such as changing wind direction or the frequency of storms, could likewise be expected to have widespread impact on the system, and emerge as broad-scale patterns in multivariate analyses. In the present work, we focus on temperature effects.

A cursory analysis of ocean model output typically reveals broad-scale patterns which appear to strengthen and weaken synchronously with a major forcing variable. In addition, we may notice that certain physical and biological variables tend to rise and fall together. A formal statistical evaluation of model output can be used to quantify the response of single variables over the entire model domain. An analysis of the spatial covariance in gridded data is frequently accomplished using empirical orthogonal functions (EOFs), which compactly include most of the total variance of the system within a few dominant temporal and spatial modes (Preisendorfer, 1988). However, for a complex biophysical model, the covarying changes among different state variables of the system may be of even greater interest (Allen and Somerfield, 2009). With multivariate EOFs, we may examine the covariance structure not only across space and time, but also across state variables. The method deployed here is essentially a form of combined principal component analysis (CPCA; Bretherton et al., 1992). Where possible, a similar analysis can be applied to real data, as a stringent test of model (and data) performance. These methods will be explored more fully in Section 2.4.

1.3. Organization of this paper

We begin with a description of the methods used for the physical and biological modeling of this ecosystem, the data used for comparison with the models, and the statistical methods used for the multivariate analysis of models and data. This is followed by a description of basic features of the model output as compared with data, a limited multivariate analysis over a 6-year period where both model and data overlap, and the more extensive multivariate analysis using multidecadal model runs.

2. Methods

2.1. The physical model

2.1.1. Model structure, forcing, and boundary conditions

The physical model used here is based on an implementation of the regional ocean modeling system (ROMS) for the Northeast Pacific (NEP-5) as described by Danielson et al. (2011; henceforth referred to as DCHWS). ROMS is a sigma-coordinate model with curvilinear horizontal coordinates; a description of basic features and implementation can be found in Haidvogel et al. (2008) and Shchepetkin and McWilliams (2005). The NEP-5 grid has approximately 10 km horizontal resolution, with 60 vertical levels. Fine-scale bathymetry is based on ETOPO5 and supplementary datasets as described in DCHWS; smoothing of that bathymetry was utilized for numerical stability. Any regions shallower than 10 m were set to be 10 m deep. Mixing is based on the algorithms of Large et al. (1994). Both ice (Budgell, 2005) and tidal dynamics are included in this model; the explicit inclusion of tidal flows allows tidally generated mixing and tidal residual flows to develop. Freshwater runoff was applied by freshening of the salinity field within a few gridpoints of the coastline, using the monthly runoff values of Dai et al. (2009). Bulk forcing, based on algorithms of Large and Yeager (2008), was used to relate winds, air temperature, relative humidity, and downward shortwave and longwave radiation to surface stress and the net transfers of sensible heat, latent heat, net shortwave and net longwave radiation through the sea surface. The simulation detailed in DCHWS covers the period 1970–2004, which includes substantial interannual and interdecadal variability.

For the present work we utilized three forcing datasets, with the intent of spanning the years 1970–2009 (hindcast) and 2010–2040 (forecast). The common ocean reference experiment reanalysis (CORE; Large and Yeager, 2008) was utilized for a hindcast of years 1969–2004. The climate forecast system reanalysis (CFSR; Saha et al., 2010) was utilized for a hindcast of years 2003–2009. The coupled global climate model (CGCM3) from the Canadian Centre for Climate Modelling and Analysis (Flato et al., 2000) was utilized for a forecast of years 2003–2040. Note that CORE is a global atmospheric reanalysis spanning 1950–2004, while CFSR is a coupled atmospheric and oceanic reanalysis spanning 1979–present. Use of the CORE product for most of our hindcast is based on the availability of CORE forcing variables for the earlier decades, as well as its broad acceptance within the oceanic community. CORE products were not available for years beyond 2005 at the time our analyses were begun, while CFSR products were not available for years before 1979; hence both were employed for different portions of our hindcast. Overlapping runs for 2003 and 2004 allowed a comparison of results using the two reanalyses; these were used to adjust CFSR for compatibility with CORE. Ultimately our "continuous" (i.e. concatenated) hindcast/forecast series was composed of the CORE results for 1970–2004, CFSR results for 2005–2009, and CGCM3 results for 2010–2040.

The CGCM3 forecast (specifically, CGCM3.1-t47, under emissions scenario A1B) is one of the Intergovernmental Panel on Climate Change (IPCC) models used to explore the coupled global atmospheric and oceanic response to anticipated changes in atmospheric CO2. CGCM3 makes use of the same ocean component as that used in the earlier CGCM2 (Flato et al., 2000), but

Please cite this article as: Hermann, A.J., et al., A multivariate analysis of observed and modeled biophysical variability on the Bering Sea shelf: Multidecadal.... Deep-Sea Res. II (2013), http://dx.doi.org/10.1016/j.dsr2.2013.04.007

employs a substantially updated atmospheric component. Hindcasts with the CGCM3 model have demonstrated fidelity to present mean conditions in the Bering Sea (Wang et al., 2010); hence it was selected as one of the several IPCC forecasts to use in downscaling runs. Note that whereas CORE and CFSR are reanalyses based on the data, the CGCM3 is a free-running forecast beyond 2001, and hence does not capture the details of interannual variability during 2003–present. This necessarily results in a degree of discontinuity between our CFSR and CGCM3 results at the beginning of 2010.

For CORE- and CFSR-based runs, we utilized 6-hourly values for wind speed, temperature, humidity and sea-level pressure, and daily average values for shortwave and longwave radiation (the model internally converts daily shortwave into instantaneous values). CORE provided monthly values for rainfall; for CFSR we used 6-hourly values. For CORE-based runs, the monthly runoff estimates of Dai et al. (2009), available for 1948–2007, were used near coastal boundaries. For CFSR, we utilized a monthly climatology of runoff values based on the Dai et al. (2009) timeseries. For CGCM3-based runs we utilized the available daily average values of all atmospheric forcing values, and the same runoff climatology as for CFSR. These attributes of the runs are summarized in Table 1.

A subset of the NEP-5 domain was utilized for our Bering Sea biophysical simulations; this grid is henceforth referred to as Bering10K. The domain is shown in Fig. 1. For the CORE-based hindcast, initial and lateral boundary conditions were obtained from the NEP-5 simulation of DCHWS (itself driven by CORE forcing, with initial and boundary conditions from the SODA v2.0.2 reanalysis, Carton and Giese, 2008). For the CFSR-based hindcast, hourly values from the CFSR ocean model (http://nomads.ncdc.noaa.gov/data.php#cfs-reanal) were filtered to 5-day averages for use as boundary conditions. This is the same time averaging used for the SODA BCs in DCHWS. For the CGCM3-based forecast, monthly averaged properties from CGCM3 ocean model were used as boundary conditions. All the boundary conditions were enforced using the hybrid nudging/radiation scheme of Marchesiello et al. (2001). The hindcast using CFSR boundary and atmospheric forcing, and the forecast using CGCM3, were both initialized in January 2003 from CORE output, so as to overlap the CORE hindcast during 2003–2004. After calibration of shortwave and longwave fluxes (see Section 2.1.2), no significant differences were found between the CORE and CFSR hindcasts of the Bering Sea during these 2 years. As in DCHWS, outflow through the Bering Strait was fixed to a value of 0.8 sv.

The full 60-level vertical resolution of Bering10K has been used for multiyear simulations of biophysical dynamics of the Bering Sea (Gibson et al., unpublished). Here, to facilitate the execution of long multidecadal biophysical runs, we have reduced the vertical resolution from 60 to 10 levels. We fully recognize the desirability of greater vertical resolution; the use of only 10 levels inevitably degrades the resolution of features such as the seasonal pycnocline and the subsurface chlorophyll maximum. However, as shown in the Results section, this reduced version still retains most of the essential physical and biological dynamics, as well as model-generated relationships among physical and biological qualities. This makes it a very useful (albeit imperfect) tool to investigate the interannual variability of the entire system, the covariance among different elements of the system, and the spatial relationships of that covariance over multiple decades.

2.1.2. Calibration of the physical model

While our Bering10K physical model is very similar to that used in DCHWS, certain aspects were calibrated to better fit the observed temperature and salinity fields of the Bering Sea. These include the following:

1. Sensible and latent heat fluxes, calculated through the Large and Yeager (2009) algorithms, were increased by 25% each. This was found necessary to keep the water column from overheating during the summer months, in response to absorption by shortwave radiation (this bias was evident in both 60- and 10-layer versions of the model, e.g. see Fig. 8 of DCHWS). Reasonable justifications for this change include the extreme roughness of the sea surface in the Bering Sea, which could result in significant heat transfer due to sea spray (Andreas et al., 2008), and the fact that most bulk flux algorithms were initially developed using equatorial and mid-latitude data, rather than subpolar and polar data.
2. The latitude-dependent open-ocean albedo of the Bering Sea surface was increased from ~0.075 to ~0.15. As in (1), this was found necessary to reduce excessive summer temperatures, which are largely driven by the shortwave flux. Reasonable justifications for this change include the prevalence of whitecaps (which reflect sunlight) in the Bering Sea. In general, observed open-ocean albedo is higher at high latitudes than in the tropics (Large and Yeager, 2009). The adjustment of albedo,

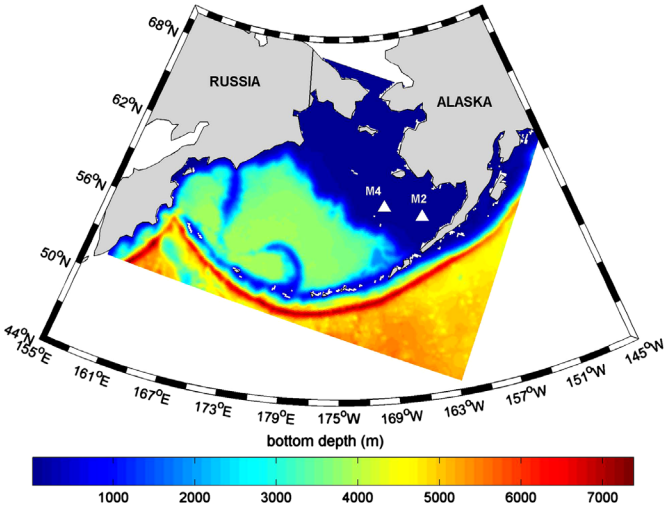

Fig. 1. Model domain with shaded bathymetry (m). The locations of biophysical moorings M2 and M4 are shown.

Table 1
Time resolution of forcing and boundary variables for the three runs. Tair=air temperature (°C); Pair=sea level pressure (mb); Qair=specific humidity (kg kg^{-1}); sward=shortwave radiation (W m^{-2}); lwrad=longwave radiation (W m^{-2}); Uwind, Vwind=eastward and northward wind velocity (m s^{-1}); Rain=rainfall (m s^{-1}); Runoff=coastal runoff (m s^{-1}); BCs=physical oceanic boundary conditions.

Run	Tair	Pair	Qair	swrad[a]	lwrad	Uwind, Vwind	Rain	Runoff[b]	BCs
CORE (1969–2004)	6 h	6 h	6 h	1 d[a]	1 d	6 h	1 mo	1 mo	5 d
CFSR (2003–2009)	6 h	6 h	6 h	1 d[a]	1 d	6 h	6 h	1 mo	5 d
CGCM3 (2003–2040)	1 d	1 d	1 d	1 d[a]	1 d	1 d	1 d	1 mo	1 mo

[a] sward is converted to instantaneous values (based on solar altitude) in ROMS.
[b] CORE uses monthly runoff estimates; CFSR and CGCM3 use monthly climatology.

rather than incident shortwave radiation per se, was based on a comparison of shortwave measurements at station M2 with the downward shortwave forcing in CORE; the two were found in good agreement, i.e. CORE does not appear to overestimate shortwave as had been found with earlier NCEP results (Ladd and Bond, 2002). A second possible factor, which could reduce the conversion of incident shortwave radiation to heat in the water column, is the absorption of photons via the intense primary production of the Bering Sea. A rough calculation suggests this may be a significant loss (as much as 10 W/m^2 of energy in mid-summer), but further work is needed to quantify this term.

3. Sea surface salinity is relaxed to climatological values as in DCHWS, but with a slower timescale (in DCHWS 2 months; here 1 year), to allow more interannual variability.
4. Water column thickness in ROMS is limited to be no thinner than 0.1 m above the sea bottom, to ensure numerical stability.
5. A comparison of CFSR and CORE data for overlapping years revealed small differences in both shortwave and longwave components of the forcing. Based on a comparison of CORE and CFSR values for 2002–2006, the CFSR downward shortwave was attenuated by 10%, and the CFSR downward longwave was attenuated by 3%, prior to its use as atmospheric forcing.
6. The DCHWS model utilized a time-invariant river discharge, applied as a spatially dependent surface flux. Here, the monthly and interannually varying discharge values of Dai et al. (2009) were used for this purpose; these yield an improved fit with salinity data. Where data were not available (beyond 2004), a monthly climatology based on the available record was applied.

2.2. The biological model

The biological model used here is described in Gibson and Spitz (2011). Univariate comparisons with temperature and nutrient data will be described elsewhere (Gibson et al., unpublished). The major components of this model are: nitrate, ammonium, iron, small phytoplankton, large phytoplankton, microzooplankton, small copepods, large copepods (e.g. *Neocalanus* spp.), krill (euphausiids), jellyfish, ice phytoplankton, iron, nitrate, ammonium, slow sinking detritus, fast sinking detritus, benthic detritus, and benthic infauna. These components are summarized in Fig. 2. While the present work concerns only the lower trophic level dynamics of the system, other simulations couple these with a size- and age-structured fish model (FEAST; Aydin et al., unpublished) to examine both top-down and bottom-up control of zooplankton.

As with surface salinity, a small relaxation term (1 year timescale) was utilized to guide iron, nitrate, and ammonium back to climatological profiles, to prevent spurious long-term drift. Such drift is due primarily to missing elements of the nitrogen and iron cycles, which are not closed in this model. A comparison of simulations with and without this relaxation term demonstrated no appreciable difference over a 4-year period; at the same time, this small corrective term proved essential for our multidecadal runs.

2.3. Observations compared with the model

Three types of data were compared with the model: Eulerian timeseries from biophysical moorings at stations M2 (56.87N, 164.05W) and M4 (57.85N, 168.87W) along the 70 m isobaths (mid-shelf, Fig. 1), spatially gridded velocities derived from drogued Lagrangian drifter data on the shelf, and spatially gridded hydrographic and chlorophyll data from repeated surveys.

The biophysical mooring data have been described in a series of papers by Stabeno et al. (2001, 2007, 2010, 2012a, 2012b). A nearly continuous multiyear series of temperature, salinity, and currents, spanning the water column, has been maintained at M2; similar (albeit less complete) series have been maintained at locations further north along the 70 m isobaths (e.g. M4). Winds and solar insolation have been measured continuously at M2 during many of these years. While salinometer data are sparser than thermistor data, the combined data were sufficient to generate estimates of water column stability. As in Ladd and Stabeno (2012), we used the potential energy anomaly ϕ, which is the amount of energy required to completely mix the water column (Simpson et al.,

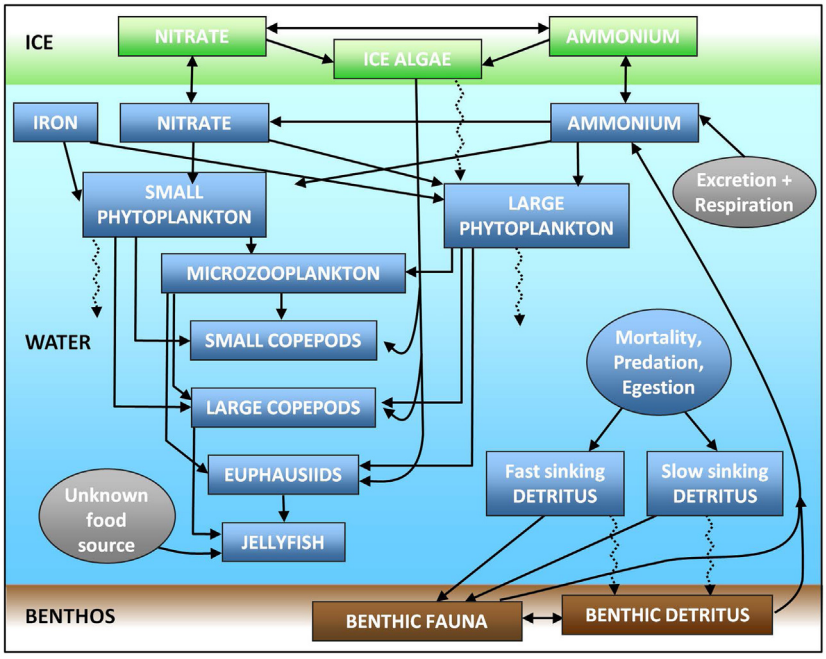

Fig. 2. Structure of the NPZ model used in this study (from Gibson and Spitz, 2011).

1978):

$$\phi = \frac{1}{h}\int_{-h}^{0}(\rho-\overline{\rho})gz\,dz; \quad \text{where } \overline{\rho} = \frac{1}{h}\int_{-h}^{0}\rho\,dz. \tag{1}$$

The same formula was applied to model output, for comparison with the Ladd and Stabeno (2012) values at M2.

Based on time- and depth-averaged temperature at M2, the years are divided into three categories: cold (1995, 1997, 1999, 2007–2010); average (1996, 2000, 2006); and warm (1998, 2001–2005). This classification is based on Stabeno et al. (2012a). Using this classification of years, we compare measured velocities at M2 with their model equivalent at near-surface (10–15 m) and near-bottom (50–55 m) locations.

We also compare climatological velocities from drogued drifter data with their model equivalent on the Bering Sea shelf. Our basic methodology for drifter data is similar to that described in Stabeno and Reed (1994). Drifters were outfitted with holey-sock drogues and tracked via satellite. Data were available for years 1995–2006; hourly changes in drifter position were used to calculate the local velocity. Model climatology was derived from 1986 to 2004 of the CORE-forced hindcast. Both model and drifter data from May 15 to October 15 of each year were binned using the same, regular $0.5^\circ \times 0.5^\circ$ latitude–longitude grid. From the data, only those bins with a total of at least 200 hourly drifter observations were retained for comparison (note this can be from a single drifter over 200 h, or many drifters over shorter periods). Further, only those locations shallower than 200 m are compared; observations were too sparse beyond the shelf break to obtain stable mean values at the $0.5^\circ \times 0.5^\circ$ resolution, due to intermittent shelf-break eddies in both model and data.

Hydrographic surveys conducted under the BASIS program are used in the multivariate analysis. BASIS data include observations of temperature, salinity, nutrients, phytoplankton, zooplankton, and fish, obtained between mid-August and early October from 2002 to present. In the present work, we utilize only the temperature, salinity, and total chlorophyll data, which were available as gridded fields for years 2003–2009. The sampling grid covers the eastern Bering Sea shelf from 55N to 65N; grid spacing is approximately 55 km. Station locations and other details of BASIS methodology are described in Danielson et al. (2010, 2011).

2.4. The multivariate statistical analysis

While multivariate statistics are routinely applied to biological data, with few exceptions (e.g. Allen and Somerfield, 2009) they have not been applied to biophysical model output. Here we provide a brief description of our multivariate method and its potential value. In physical oceanography and meteorology, EOFs are used as a standard tool to relate change in one part of the fluid to changes in some other part—for example, a correlation in the rise and fall of SSH in different parts of the ocean, driven by broad-scale winds. EOFs are the most compact way of expressing the common variance of a collection of timeseries, as they are the eigenfunctions of the matrix of covariances among all the series (Preisendorfer, 1988). Typically they are applied using timeseries of a single variable at multiple locations:

$$T(x_1,t_1), T(x_1,t_2), T(x_1,t_3), \ldots\ldots T(x_1,t_N) \tag{2a}$$

$$T(x_2,t_1), T(x_2,t_2), T(x_2,t_3), \ldots\ldots T(x_2,t_N) \tag{2b}$$

$$T(x_M,t_1), T(x_M,t_2), T(x_M,t_3), \ldots\ldots T(x_M,t_N) \tag{2c}$$

In biology, principal component analysis is frequently used to establish the co-occurrence of species from a collection of samples at one location:

$$N(x_1,t_1), N(x_1,t_2), N(x_1,t_3), \ldots\ldots N(x_1,t_N) \tag{3a}$$

$$P(x_1,t_1), P(x_1,t_2), P(x_1,t_3), \ldots\ldots P(x_1,t_N) \tag{3b}$$

$$Z(x_1,t_1), Z(x_1,t_2), Z(x_1,t_3), \ldots\ldots Z(x_1,t_N) \tag{3c}$$

or a set of multivariate observations scattered in space and time (e.g. Allen and Somerfield, 2009)

$$N(x_1,t_1), N(x_2,t_2), N(x_3,t_3), \ldots\ldots N(x_M,t_M) \tag{4a}$$

$$P(x_1,t_1), P(x_2,t_2), P(x_3,t_3), \ldots\ldots P(x_M,t_M) \tag{4b}$$

$$Z(x_1,t_1), Z(x_2,t_2), Z(x_3,t_3), \ldots\ldots Z(x_M,t_M) \tag{4c}$$

where N, P, Z represent three different biological properties, e.g. nutrients, phytoplankton, and zooplankton.

Note how in (3a)–(3c), the different variable types are analogous to the different spatial locations used in (2a)–(2c). In either case the fundamental goal is the same; to compactly describe the covariance among a collection of timeseries. To this end, a $N \times N$ matrix is constructed whose elements are the covariance (or correlation) of the ith series to the jth timeseries for all $i=1,\ldots N$ and $j=1,\ldots N$. The eigenvectors and eigenvalues of this matrix are derived; the eigenvectors are then interpreted as coupled modes of variability among the series. For EOF analysis, this results in an orthogonal set of spatial patterns (the "modes") and an orthogonal set of timeseries (the principal components, i.e. PCs).

Since our aim here is the examination of coupled spatial modes of biophysical variability, we use a multivariate set of timeseries spanning the model domain:

$$\begin{array}{l} N(x_1,t_1),\ N(x_1,t_2),\ N(x_1,t_3),\ldots\ldots N(x_1,t_N) \\ P(x_1,t_1),\ P(x_1,t_2),\ P(x_1,t_3),\ldots\ldots P(x_1,t_N) \\ Z(x_1,t_1),\ Z(x_1,t_2),\ Z(x_1,t_3),\ldots\ldots Z(x_1,t_N) \\ T(x_1,t_1),\ T(x_1,t_2),\ T(x_1,t_3),\ldots\ldots T(x_1,t_N) \\ \ldots\ldots\ldots\ldots\ldots\ldots\ldots\ldots\ldots\ldots\ldots\ldots\ldots\ldots\ldots\ldots \\ N(x_M,t_1),\ N(x_M,t_2),\ N(x_M,t_3),\ldots\ldots N(x_M,t_N) \\ P(x_M,t_1),\ P(x_M,t_2),\ P(x_M,t_3),\ldots\ldots P(x_M,t_N) \\ Z(x_M,t_1),\ Z(x_M,t_2),\ Z(x_M,t_3),\ldots\ldots Z(x_M,t_N) \\ T(x_M,t_1),\ T(x_M,t_2),\ T(x_M,t_3),\ldots\ldots T(x_M,t_N) \end{array}$$

Again, the intended product is the covariance structure of the coupled system—that is, which features of the biological and physical system covary, and what is the spatial structure of this covariance. At the outset, we expect that none of the multivariate modes from this analysis will explain as much of the variance contained a *single* variable, as can be explained through univariate EOF analysis. However, this approach is a useful way to summarize the spatial modes in which different hydrographic features and trophic levels rise and/or fall together, either through self-generated dynamics (e.g. phytoplankton decrease as zooplankton increase) or through a common driver (warmer temperatures lead to increased/decreased production of certain trophic levels in particular areas). For the Bering Sea, shifts to the north and/or inshore are of particular interest.

It is important in such an analysis to avoid the pitfall of quadrature. As an example, when control is neither fully top-down nor fully bottom-up, a biological system (real or modeled) may develop predator–prey cycles (and/or seasonal succession) which place predator and prey 90° out of phase with each other—that is, closely linked but perfectly uncorrelated. A simple example is a phytoplankton bloom followed with some time lag by zooplankton growth. To guard against this pitfall, we must take care to average over the timescale on which such cycles would occur. For the full multivariate analysis of Section 3.3.2, we use

multiyear timeseries composed of annual averages for each variable and location.

Note also the need for normalization of the timeseries prior to analysis; each variable is in different units, and we seek to give all of them an equal chance to contribute to the biophysical modes. Here, we proceed by normalizing each variable using its standard deviation over all space and time. This simultaneously eliminates units and emphasizes the relative change in each case. Once the EOFs are calculated on these normalized series, we de-normalize the results by multiplying back by the set of standard deviations. The results are then plotted using shading levels ranging from −1 to +1 s.d. of each variable. In this manner, we illustrate how strongly each of the variables has contributed to the coupled mode, relative to that variable's own total variance.

Many timeseries could be used as input for this type of multivariate analysis, up to the full 3D fields of every modeled variable, as well as the many fluxes among those variables. For the present investigation, we select some of the major scalar variables which are believed to play a role in the OCH, with a focus on temperature, ice, and zooplankton. We further limit our attention to 2D variables (e.g. ice cover), 2D slices from 3D variables (sea surface and sea bottom temperature), or vertical averages of 3D variables (e.g. zooplankton).

Two types of analysis were performed:

1) A direct comparison with BASIS data was carried out for sea surface temperature, sea bottom temperature, sea surface salinity and averaged phytoplankton in the upper 40 m. Model-equivalent values from the CFSR-forced hindcast were sampled at precisely the same locations and times as the BASIS data for this comparison (sampled days span mid-August–early October of each year). A carbon-to-chlorophyll ratio of 50:1 was assumed for this analysis, to convert chlorophyll values (from BASIS surveys) to large plus small phytoplankton biomass (from the model output). A summary of the variables used for this analysis is shown in Table 2. Extensive gridded data do not exist for other seasons, however, univariate comparisons with physical and biological have quantified the correspondence to observed temperature and nutrient fields in most areas (Gibson et al., unpublished).
2) An extended multiyear analysis was carried out using annual averages of 15 properties from the model output, chosen to include features relevant to the OCH hypotheses (temperature, ice, nutrients, and multiple trophic levels). A summary of the variables used for these analyses is shown in Table 3. This more extensive multivariate analysis was applied to three different groupings of the simulation output: (1) a concatenated series of CORE (1970–2004) and CFSR (2005–2009) hindcasts; (2) last two decades of the CGCM3 forecast (2020–2040); (3) a concatenated series of CORE (1970–2004), CFSR (2005–2009) and CGCM3 (2010–2040).

After their de-normalization, the multivariate EOFs may be interpreted as coupled spatial patterns for each of the variables, describing how particular quantities rise and/or fall together. The principal component timeseries for that mode, multiplied by the de-normalized EOF, indicates a time history of rising/falling quantities in the domain, in the original units of the variable. A spatial map for temperature with both positive and negative values indicates that, for that particular multivariate EOF, some parts of the domain rise in temperature at the same time that other parts fall in temperature, e.g. those different regions are negatively correlated. In the same way, at a particular location, we may see that temperature has positive EOF value while salinity has a negative EOF value. This indicates that those variables are negatively correlated at that location. Further, we may observe that temperature has a positive EOF value at location A, while nitrate has a negative EOF value at location B. This indicates that temperature at location A is negatively correlated with nitrate at location B.

3. Results

3.1. 10-Level physical model performance

A detailed statistical analysis of the 60-level biophysical model performance has demonstrated significant model skill in capturing the spatial and temporal variability of both temperature and nitrate in the top 40 m of the water column (Gibson et al., unpublished). The broad structure and seasonality of the nutrient field are similar in both 60-layer and 10-layer models. A thorough assessment of the 60-level physical model on the NEP-5 grid is reported in DCHWS; these included a comparison of observed vs. modeled ice and tides. As described in Section 2, our physical model is similar in structure to that of DCHWS, albeit on a smaller grid (a subsection with the same horizontal resolution as the full NEP-5 grid), and with some modifications pertaining to surface

Table 2
Variables used in the multivariate analysis of the BASIS data, and its model equivalent.

Surface temperature	SST	°C
Bottom temperature	SBT	°C
Surface salinity	SSS	psu
Phytoplankton (top 40 m ave)	PHYT	mg C m^{-3}

Table 3
Variables used in the multivariate analysis of the simulations.

Surface temperature	SST	°C
Bottom temperature	SBT	°C
Surface salinity	SSS	psu
Ice cover	ICECOVER	fractional area
Mixed layer depth	MLD	m (positive up coordinates; hence negative change denotes *deepening* MLD)
Vertical mixing (depth ave)	AKTS	m^2 s^{-1}
Nitrate+ammonium (depth ave)	NUT	mg N m^{-3}
Ice phytoplankton (surface layer ave)	ICEPHYT	mg C m^{-3}
Small plus large phytoplankton (depth ave)	PHYT	mg C m^{-3}
Microzooplankton (depth ave)	MZOO	mg C m^{-3}
Small copepods (depth ave)	COPE	mg C m^{-3}
Neocalanus (depth ave)	NCA	mg C m^{-3}
Euphausiids (depth ave)	EUP	mg C m^{-3}
Benthic detritus	BENDET	mg C m^{-2}
Benthic infauna	BENINF	mg C m^{-2}

heat flux. Here, we describe representative properties of the 10-level model, and their comparison with data. Our intent is to demonstrate that the 10-level model, while vertically coarse, captures enough of the essential physics and biology of the region to be useful as a tool to explore relevant aspects of past and future interannual change. Ice and tidal results were in fact very similar to those of DCHWS; here instead we focus on velocity, temperature and salinity results.

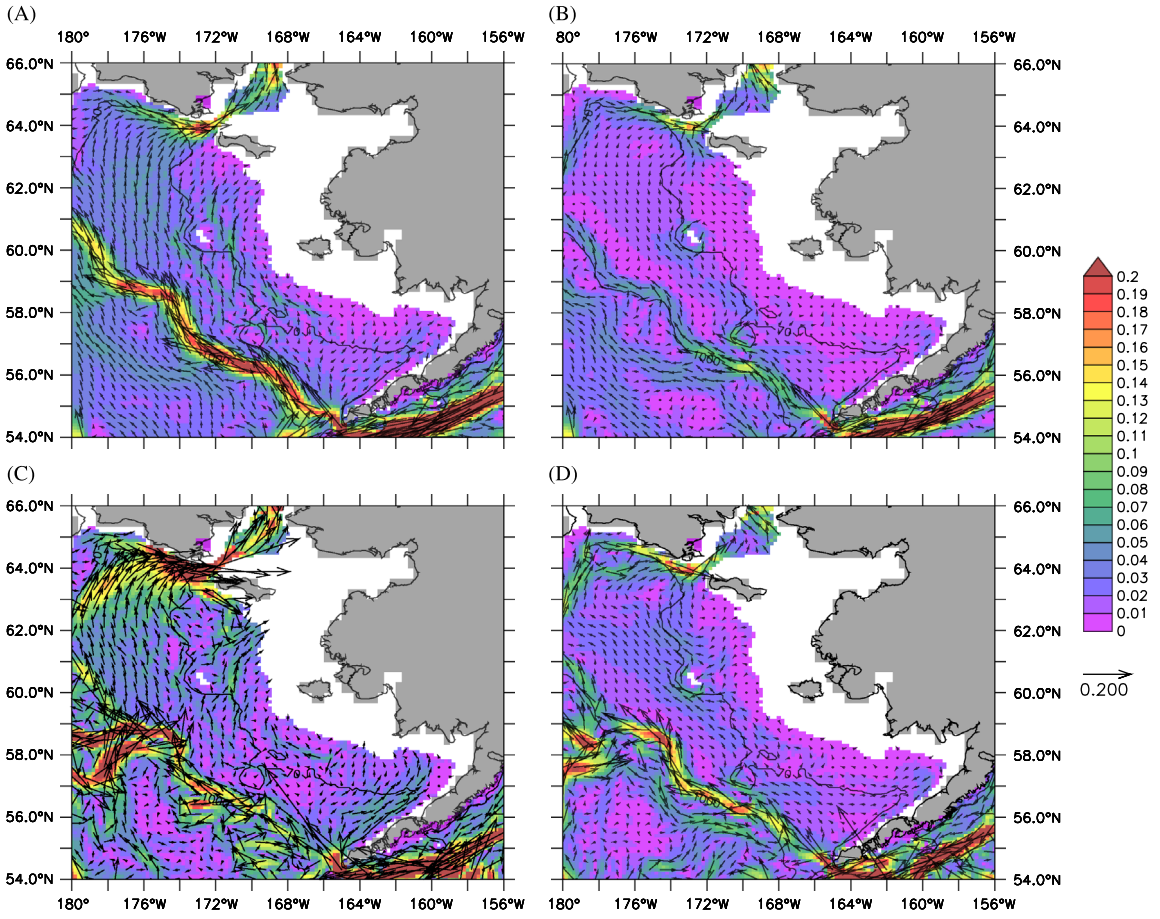

Fig. 3. Climatological and weekly averaged model velocities at 40 m, from a simulation of years 1970 to 2009. Speed is shaded (m s^{-1}). Upper panels show climatological January (A) and July (B) values; lower panels show a weekly average from January 2004 (C) and July 2004 (D). Bathymetric contours at 70 m and 1000 m depth are shown. (a) January climatology, (b) July climatology, (c) 11 Jan 2004 and (d) 11 July 2004.

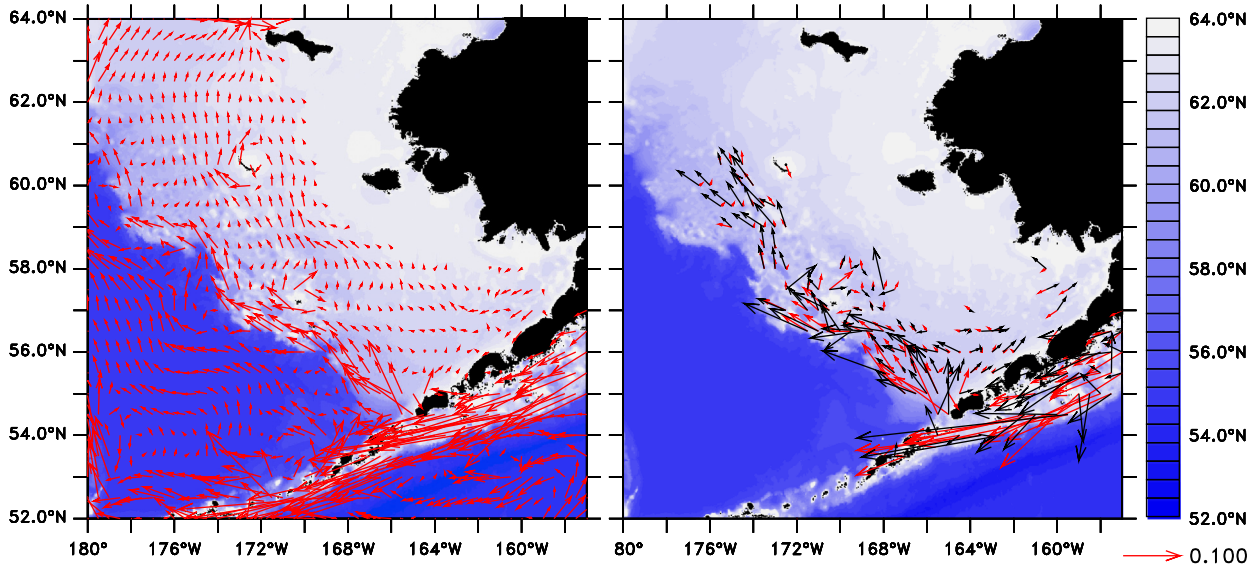

Fig. 4. Climatological modeled (red) vs. measured (black) summer (May 15–October 15) velocities at 40 m depth for the Bering Sea. Velocities are in m s^{-1}; bathymetry is shaded (m). Measured values are derived from drogued drifter climatology. Left figure illustrates model vectors (red); right figure illustrates measured (black) and modeled (red) vectors, and excludes locations with no measurements. (For interpretation of the references to color in this figure caption, the reader is referred to the web version of this article.)

Please cite this article as: Hermann, A.J., et al., A multivariate analysis of observed and modeled biophysical variability on the Bering Sea shelf: Multidecadal.... Deep-Sea Res. II (2013), http://dx.doi.org/10.1016/j.dsr2.2013.04.007

3.1.1. Climatological circulation

The climatological circulation of the model exhibits major observed circulation features between 54N and 66N: a vigorous flow along the southern boundary of the Aleutians and through Unimak Pass, and to the northwest along the shelf break (Fig. 3). Weaker but persistent flows are to the northwest on the Bering Sea shelf; these are strongest in winter. Weekly averaged velocities exhibit more detailed structures, such as 200-km eddies along the shelf break. Note how the climatological maps reveal strong northwestward flows along the 50 m and 100 m isobaths in winter; these correspond to frontal structures separating the inner/middle and middle/outer biophysical regimes of the Bering Sea (Coachman, 1986; Kachel et al., 2002).

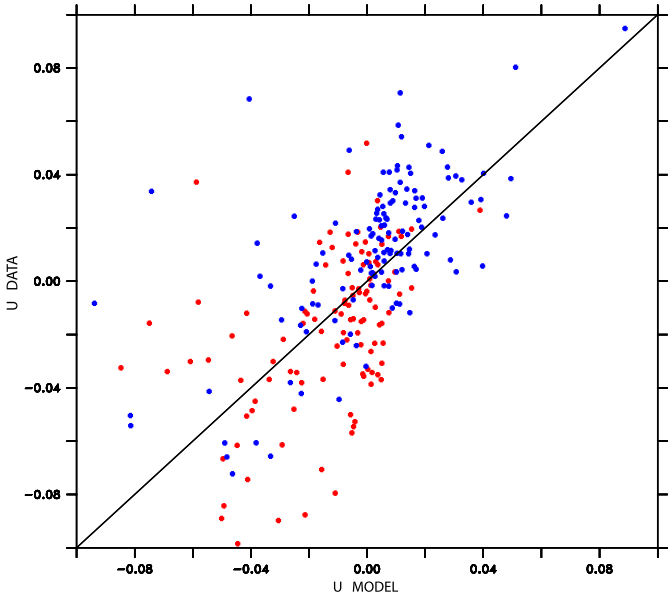

Fig. 5. Modeled (*x*-axis) vs. observed (*y*-axis) values for climatological summer eastward (red) and northward (blue) velocities at 40 m. Values are in m s^{-1}. The *r*-squared values are 0.54 and 0.70 for eastward and northward velocities, respectively. (For interpretation of the references to color in this figure caption, the reader is referred to the web version of this article.)

3.1.2. Velocity climatology from drifters

In Fig. 4 we compare modeled and drifter-derived climatological velocities at 40 m depth for Bering Sea summer (May 15–October 15). Model-derived velocities are in conformance with the available data in most areas. A scatterplot compares observed climatological velocities with their equivalent from the 10-level model (Fig. 5). The *r*-squared values are 0.54 for the eastward and 0.70 for the northward velocities, respectively. There is a slight bias towards weaker velocities in the model as compared with data.

3.1.3. Mid-shelf velocity climatology

A comparison of measured climatological velocity by month at station M2 (from Stabeno et al., 2012a) with their model equivalent (Fig. 6) reveals a similar seasonal progression in both model and data, with a tendency to offshore flow during the summer. The observed and modeled summertime near-surface offshore flow is more pronounced during cold years (Stabeno et al., 2012a).

3.1.4. Mid-shelf hydrography at stations M2 and M4

Thermistor arrays at mid-shelf stations M2 and M4 allow a detailed comparison with model output. The CORE-driven hindcast, even with only 10 vertical levels, captures the basic seasonal and interannual trends as the data (Fig. 7). Seasonal creation of the thermocline in summer is followed by its destruction in the fall. The presence of ice in cold years is

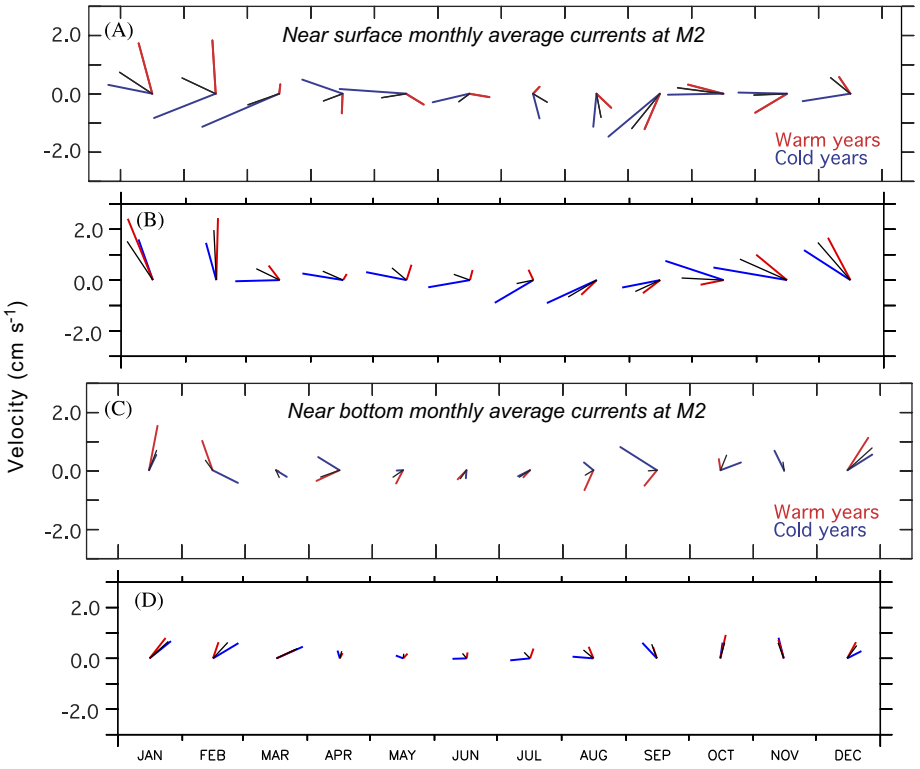

Fig. 6. Monthly velocity climatology at station M2, from observation and model. (A) Near-surface velocity from data; (B) near-surface velocity from model; (C) near-bottom velocity from data; (D) near-bottom velocity from model. Colors indicate averages from warm years only (red), cold years only (blue) and all years combined (black). (A) and (C) are adapted from Stabeno et al. (2012a). (a) surface data, (b) surface model, (c) bottom data and (d) bottom model. (For interpretation of the references to color in this figure caption, the reader is referred to the web version of this article.)

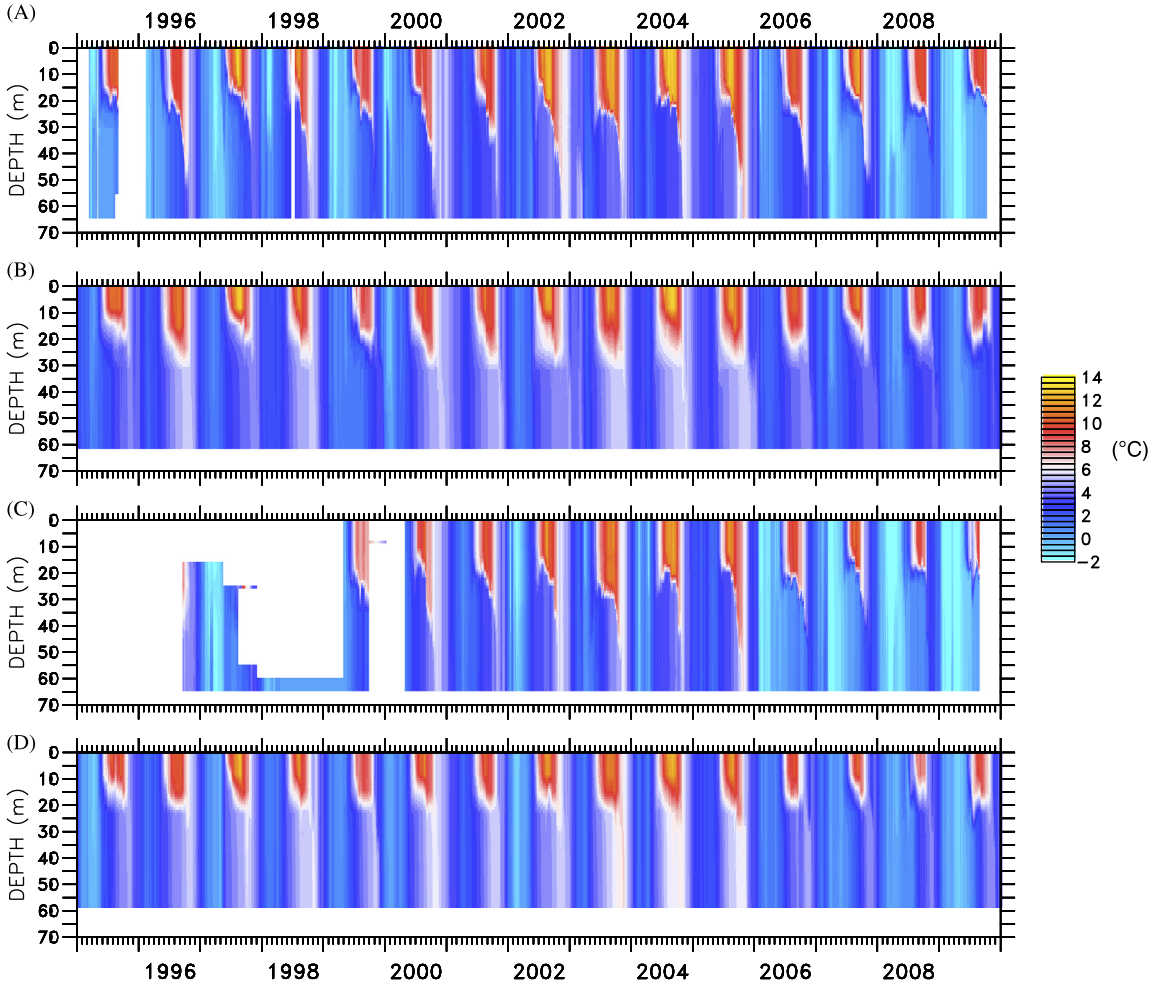

Fig. 7. Comparison of measured vs. modeled temperatures at stations M2 (A and B) and M4 (C and D). Units are °C. (a) M2 DATA, (b) M2 MODEL, (c) M4 DATA and (d) M4 MODEL.

associated with near-freezing temperatures which extend to the bottom (e.g. January–April 2009). The model exhibits similar patterns at slightly reduced amplitude. Depth-averaged temperatures are compared in Fig. 8. Model bias is smallest in summer; largest discrepancies are found in winter, where the model has a residual tendency to underestimate the areal extent of ice at both M2 and M4 (not shown). When ice coverage is not complete in a given grid cell, the average temperature there will be above freezing. A straightforward adjustment of the ice module can increase ice cover growth, as opposed to ice thickness growth, when new ice is formed; this has been applied to recent simulations and will be reported in a future paper.

Salinity at M2 and M4 has been more sparsely sampled than temperature. Rather than full vertical profiles, we compare salinity timeseries at two depths: 15 m and 55 m (Fig. 9). In both model and data, interannual variability is the dominant signal, and the residual between model and data at 15 m is frequently less than 0.1 psu. This is in fact within the accuracy of the salinometer itself. Note how the model generates a fresh, 20 m-deep surface layer in summer, especially during cold years.

The model likewise captures the essential seasonal and interannual patterns of stratification as expressed through the potential energy anomaly ϕ at station M2 (Fig. 10). Stratification increases rapidly in May and peaks around August. As with temperature itself, the model exhibits the same pattern as the data, but at slightly reduced amplitude.

3.2. Multidecadal behavior of the model

Before proceeding to the full multivariate analysis, we focus on two aspects of the interannual/interdecadal performance of the 10-level model: temperature and large crustacean zooplankton.

3.2.1. Mid-shelf temperature timeseries

Multidecadal timeseries of depth-averaged temperature at M2 from the model, based on each of the three forcing datasets (Fig. 11), exhibit marked interannual and interdecadal variability, with some pronounced changes corresponding with regime shifts of the larger North Pacific (e.g. the shift of 1976). The recent periods of warming (1999–2004) and cooling (2005–2009) (see Fig. 9) are clearly evident in the CORE and CFSR hindcasts. These two hindcasts overlap during 2003–2004; the time plots of temperature during those years show essentially identical results (and hence are difficult to distinguish as separate lines in Fig. 11). The CGCM3-based forecast indicates a slow warming trend, with the 5-year mean average gradually rising from ~3.75 °C to ~5.25 °C by the mid-2030s. Note how the CGCM3 forecast, downscaled here beginning with year 2003, anticipated a colder series of years in 2003–2006 and a warmer series of years in 2006–2010 than were actually observed. This level of mismatch is in fact anticipated, as CGCM3 is a freely evolving coupled global air–sea simulation unconstrained by data; as such it manifests different interannual details than the real atmosphere and ocean.

Please cite this article as: Hermann, A.J., et al., A multivariate analysis of observed and modeled biophysical variability on the Bering Sea shelf: Multidecadal.... Deep-Sea Res. II (2013), http://dx.doi.org/10.1016/j.dsr2.2013.04.007

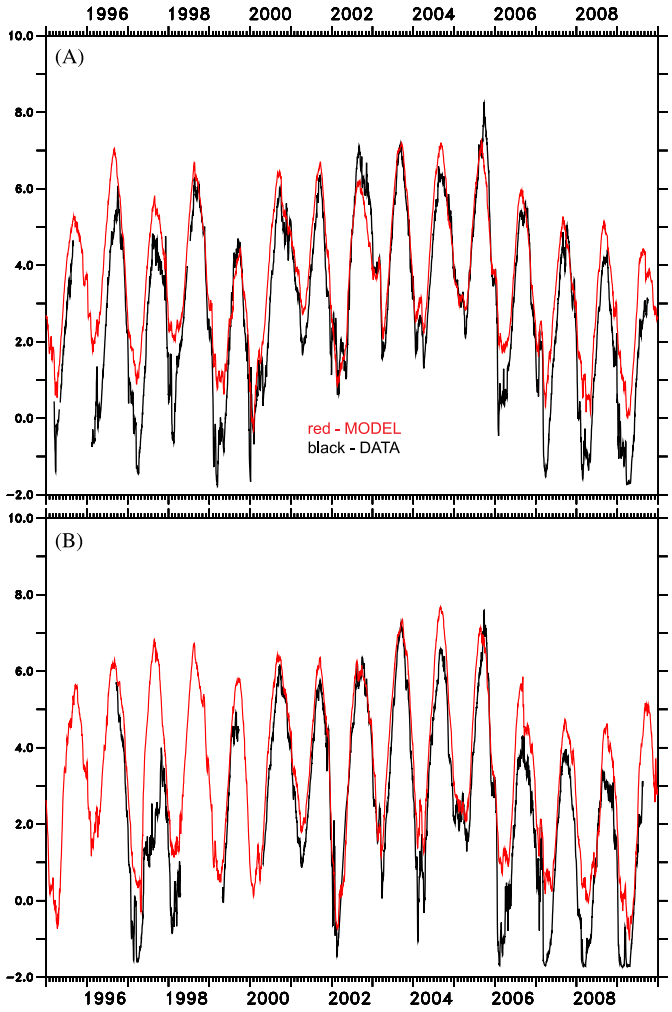

Fig. 8. Comparison of measured (black) vs. modeled (red) depth-integrated temperature at locations M2 (A) and M4 (B). Units are °C. (a) M2 depth-average T and (b) M4 depth-average T. (For interpretation of the references to color in this figure caption, the reader is referred to the web version of this article.)

3.2.2. Correlation with large crustacean zooplankton

Observations during the recent period of cooling in the Bering Sea suggest a tendency for large crustacean zooplankton (represented by euphausiids and neocalanus in the model) to covary inversely with temperature (Hunt et al., 2011; Coyle et al., 2011). This general tendency is apparent in the 10-level model results over all three simulation periods (Fig. 12), and is consistent with the detailed comparisons by region from the 60-level model during warm vs. cold years (Gibson et al., unpublished).

3.3. Results from multivariate analysis

As noted in the methods, the multivariate EOFs may be interpreted as coupled spatial patterns for each of the variables, describing how particular quantities, at particular locations, rise and/or fall together. Below we explore these patterns, and their amplitude through time.

3.3.1. Comparison with BASIS gridded data

The leading biophysical mode from the BASIS data exhibits a correlated fall in surface and bottom temperatures (SST, SBT) in the southeastern Bering Sea (Fig. 13). Higher sea surface salinity (SSS) is found along the 70 m isobaths during warmer years, and higher concentrations of phytoplankton (PHYT) are observed during those years. The leading biophysical mode from the corresponding model output exhibits markedly similar patterns in SST, SBT and SSS during warm/cold years, but a much weaker (and even negative) correlation with PHYT. The temporal trend (first PC) of this mode is markedly similar between the model and data; in both cases the dominant signal reflects the cooling between 2005 and 2009. The conformance of the model/data SSS patterns is especially striking. The likely cause of this pattern is melt along the southern/offshore extent of the seasonal ice field, as suggested in the (univariate) salinity EOF analysis of Danielson et al. (2010, 2011). In the northeastern Bering Sea, ice is typically formed in the lee of headlands and islands and is advected south by the prevailing winds (Stabeno et al., 2010), hence serving as a net conveyor of freshwater to the south. In warm years, less ice is melted along the southeast segment of the 70 m isobath (the southerly/offshore extent of this ice field), and so the SSS is higher than in cold years at that location.

3.3.2. Full multivariate analysis of model output

The full multivariate analysis of model output yields a leading spatial mode where some variables rise in concert with others (e.g. SST and SSB), whereas others vary out of phase with each other (e.g. SST vs. ICECOVER). Biological variables such as EUP show marked spatial variance; positive/negative values on the inner/outer shelf indicate that EUP goes up on the inner shelf when it is falling on the outer shelf. Further, a comparison of EUP and SST maps reveals that outer shelf EUP go down when shelf-wide SST is rising. The leading biophysical mode is similar across all groupings of the model output (Figs. 14–16). In each case, SST, SBT and SSS exhibit similar trends and tendencies as in the BASIS data. For the mode using CORE and CFSR hindcasts (Fig. 14), and the mode using all three forcing datasets (Fig. 16), warmer SST, warmer SBT, and reduced ICECOVER co-occur in the south, but *cooler* temperatures are associated with this change in the north when all three datasets are included. Increased SSS is observed at the mean location of the ice edge; these are associated with enhanced mixing (AKT) and deepening of the MLD (note: both SSH and MLD are defined in meters above mean sea level, hence more negative values for MLD denote a *deeper* mixed layer). Reduced pelagic biomass (MZOO, COPE, NCA, EUP) is found on the outer shelf, while increased biomass of those terms is found both inshore and northward. EUP in particular exhibits a decrease in biomass during warm periods, as was seen in the direct scatterplot of these quantities at M2 (Fig. 12). This inverse correlation is likewise found in the 60-level output (Gibson et al., unpublished). A similar shift is observed in benthic detritus and benthic infauna, but has a more zonal alignment (i.e., benthic biomass shifts more directly to the north, as opposed to inshore). Dissolved inorganic nitrogen (NUT) shows a trend to lower values along the 70 m isobaths when temperatures are warm; changes in large plus small phytoplankton (PHYT) are less dramatic. The amplitude of this mode (the first PC) exhibits large changes in 1975–1980, 1999–2004, and 2005–2009. These latter two periods exhibit the same interannual trends as the depth-averaged temperature timeseries at M2 (Fig. 8).

The dominant mode obtained using only the last 20 years of CGCM3-driven results (Fig. 15) are similar to those of the CORE/CFSR analysis (Fig. 14), but emphasize primarily the coupling among hydrographic variables (SST, SBT, SSS, ICECOVER). The increase in mixing and deepening of MLD are more broadly spread along the outer shelf. NUT decreases in the south and increases in the north, while PHYT increases all along the 70 m isobath; its pattern is in fact similar to that of SSS. The patterns associated with the benthos and the zooplankton are weaker than in the hindcast, and, along with the pattern for ICECOVER, have been shifted north. This likely reflects the northerly shift of the seasonal ice edge under continued warming.

When the full concatenated series (CORE/CFSR/CGCM3) is used (Fig. 16), the largest jump in the PC occurs between the end of the CFSR segment and the beginning of the CGCM3 segment.

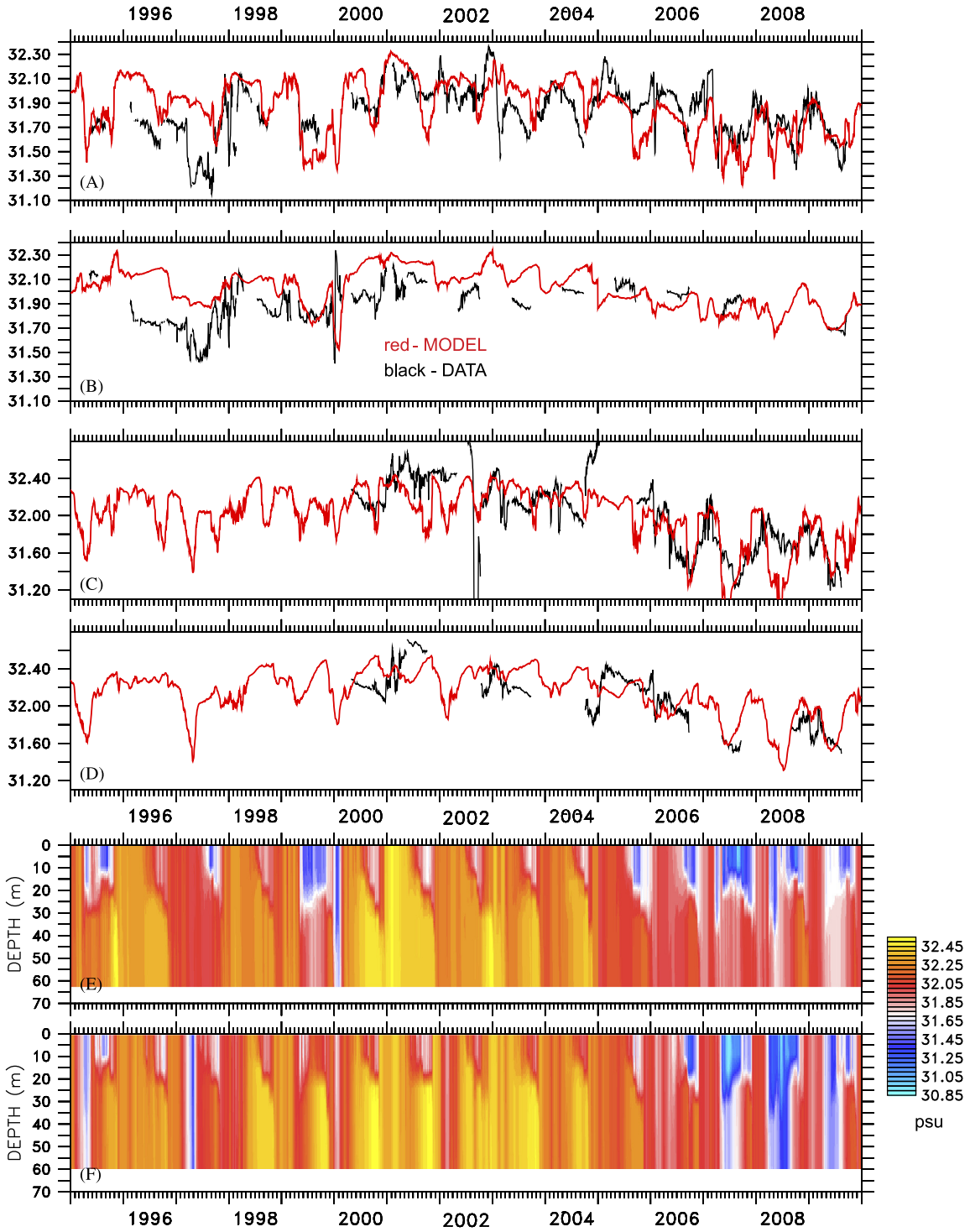

Fig. 9. Comparison of modeled vs. measured salinity at stations M2 (A and B) and M4 (C and D). Upper figures compare modeled (red) vs. measured (black) values at 15 m depth (A and B) and 55 m depth (B and D). Lower figures exhibit model values over all depths for M2 (E) and M4 (F). Units are psu. (a) M2 15 m, (b) M2 55 m, (c) M4 15 m, (d) M4 55 m, (e) M2 MODEL and (f) M4 MODEL. (For interpretation of the references to color in this figure caption, the reader is referred to the web version of this article.)

A north/south gradient in temperature (SST, SBT) is especially striking in the leading spatial mode, and emerges as well in difference maps between mean forecast and hindcast temperatures (not shown). Dissolved inorganic nitrogen (NUT) appears to contribute substantially to the dominant mode using this full concatenated series, and is positively correlated with temperature in most areas. Mixing (AKT) is diminished and the MLD shoals broadly across the shelf, in synchrony with the warmer temperature. An onshore and northward shift of pelagic and benthic biomass is once again evident, as in the analysis using CORE/CFSR only (Fig. 14).

4. Discussion

4.1. Alternate statistical approaches

It is worth considering what we gain by the CPCA analysis, that we could not learn from simple difference maps. We might see very similar patterns if we grouped the warm vs. cold years, and took the difference between those climatologies. While both approaches presume that temperature is a controlling variable, the present CPCA approach allowed its importance to more spontaneously emerge

Please cite this article as: Hermann, A.J., et al., A multivariate analysis of observed and modeled biophysical variability on the Bering Sea shelf: Multidecadal.... Deep-Sea Res. II (2013), http://dx.doi.org/10.1016/j.dsr2.2013.04.007

from the analysis, without an a priori selection of temperature categories. Further analysis will help to specify which atmospheric variables (e.g. air temperature vs. shortwave radiation) play the largest role in controlling the temperature field.

In their comparison of multivariate methods, Bretherton et al. (1992) noted that the modes produced by CPCA may exhibit a bias towards spatial structures similar to those of the most energetic univariate EOFs. In the present case, this likely means a bias towards a mode which fits much of the SST and SBT data. This is acceptable in our case, as the original intent was to seek modes which correlate with temperature. However, it is worth noting that other methods compared in Bretherton et al. (e.g. coupled correlation analysis) might produce a significantly different result. Our present usage of CPCA does appear robust, insofar as the three different choices of timeseries produced similar results.

4.2. Discrepancies with data

The primary mode computed from BASIS data exhibits correlated physical/biological properties: warmer sea surface and sea bottom temperatures, increased sea surface salinity at mean location of the ice edge, and increased phytoplankton (or more specifically, chlorophyll) on the middle shelf. While physical variables in the leading mode from the model were very similar to their BASIS data counterparts, we failed to replicate the observed positive correlation of phytoplankton with temperature. This mismatch may be due to several factors, including a bias in the timing of the modeled fall bloom as compared with the measured fall bloom (Gibson et al., unpublished). The modes computed from the longer simulations, based on annual averages of scalar properties, do appear to exhibit a positive correlation between temperature and phytoplankton on the middle shelf. The strength of this correlation varies with the span of years chosen, and is strongest when the full concatenated series (CORE/CFSR/CGCM3) is used.

The model was calibrated to better fit summer temperatures, yet there was a residual tendency of the model to overestimate winter temperature and to underestimate ice cover. The ice model itself (Budgell, 2005) contains tunable parameters, such as the

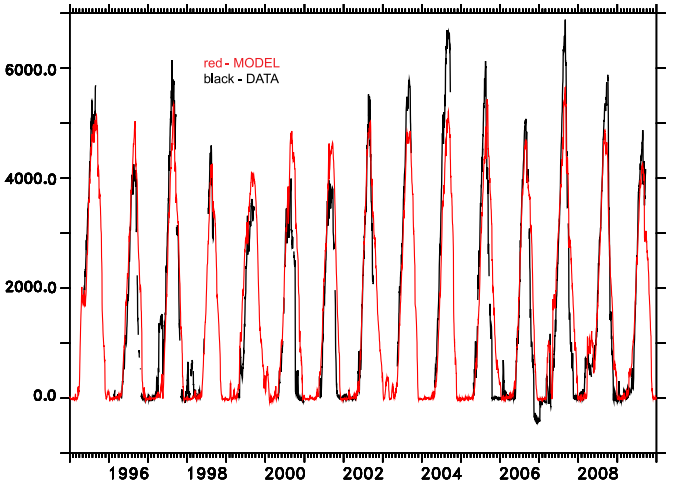

Fig. 10. Comparison of modeled (red) and measured (black) water column stability (J m^{-2}) at location M2. Measured values are from Ladd and Stabeno (2012). (For interpretation of the references to color in this figure caption, the reader is referred to the web version of this article.)

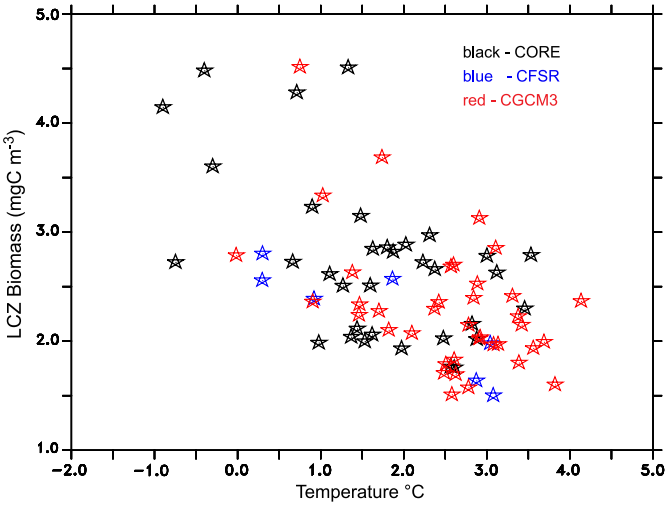

Fig. 12. Scatterplot of depth-averaged temperature (°C) in spring vs. depth-averaged large crustacean zooplankton (LCZ, mg C m^{-3}) in fall at station M2, from model hindcasts and forecast. CORE, CFSR and CGCM3 runs are marked with black, blue, and red stars, respectively. (For interpretation of the references to color in this figure caption, the reader is referred to the web version of this article.)

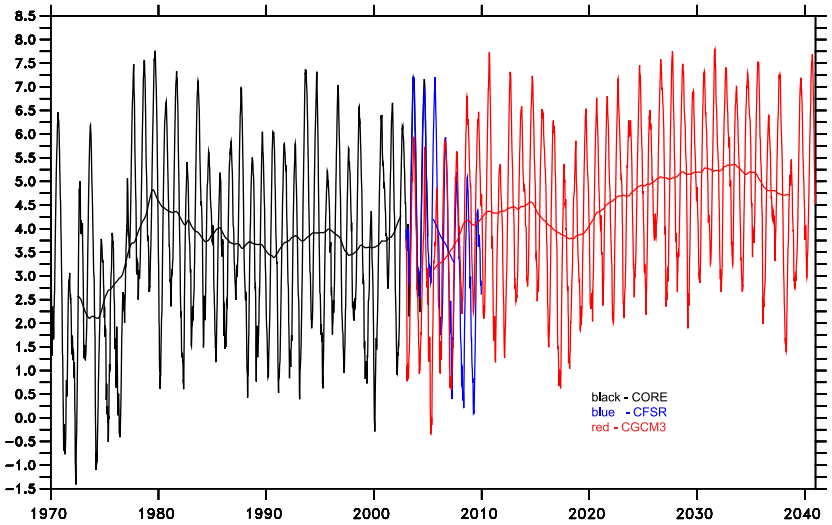

Fig. 11. Depth-averaged temperature at station M2 from model simulation using CORE hindcast forcing (black line), CFSR hindcast forcing (blue line), and CGCM3 forecast forcing (red line). Thin lines show weekly average values; thick line is 5-year running mean. Units are °C. (For interpretation of the references to color in this figure caption, the reader is referred to the web version of this article.)

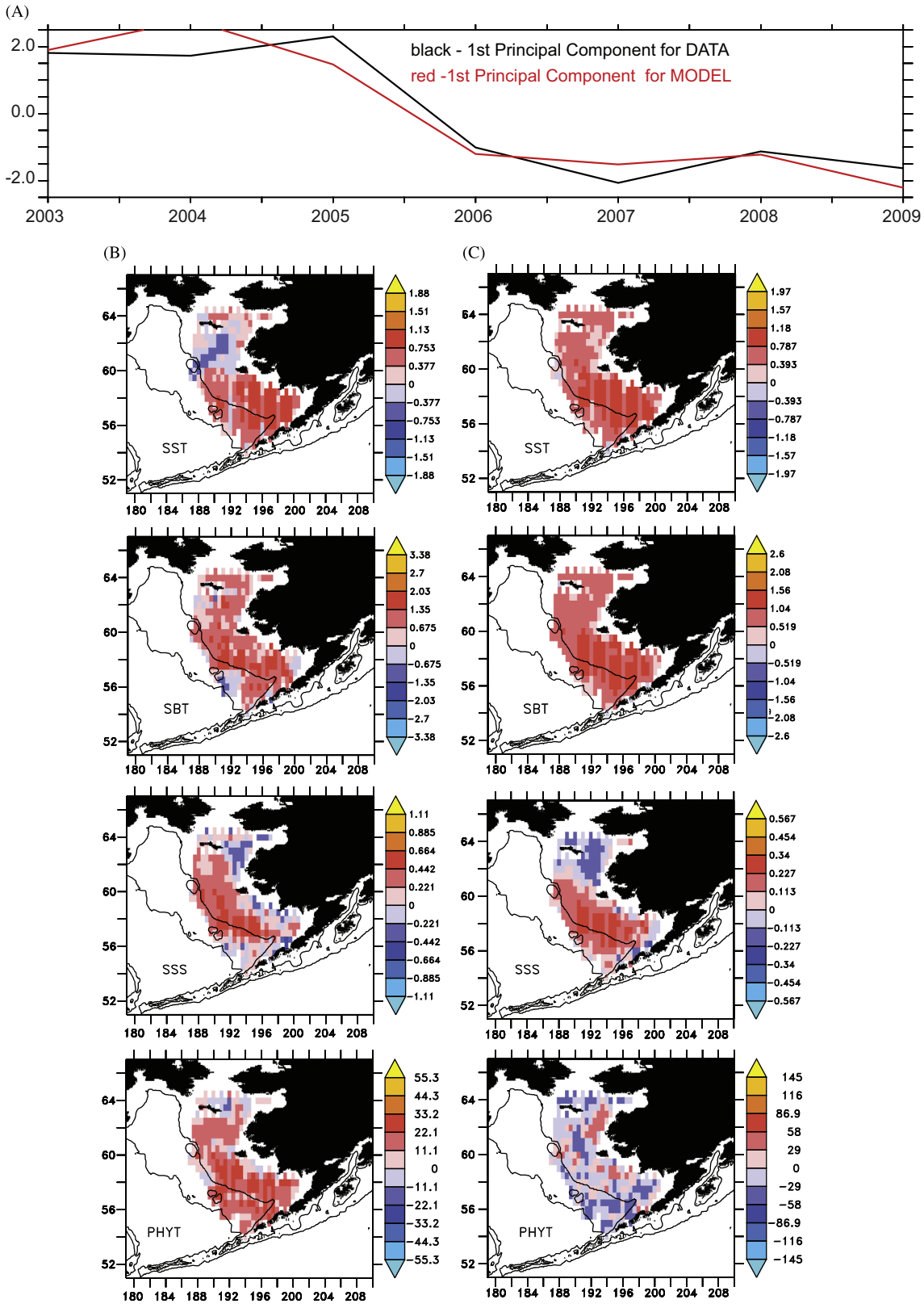

Fig. 13. Leading biophysical mode using gridded data and equivalent model output for the same variables. (A) First principal component for data (black line) and model (red line). The leading mode for data contains 43.0% of the total variance in its multivariate timeseries, and the leading mode for the model equivalent contains 49.6% of the variance in its multivariate timeseries. (B) Spatial loadings (EOFs) for each of the variables from BASIS data, converted back to their original units (listed in Table 2). Levels used for shading span −1 to +1 s.d. of each variable. Bathymetric contours at 70 m and 1000 m depth are shown. (C) Spatial loadings for each of the variables from the model, sampled at the same locations and times as the BASIS data. (a) PC1, (b) EOF1 for DATA and (c) EOF1 for MODEL. (For interpretation of the references to color in this figure caption, the reader is referred to the web version of this article.)

Please cite this article as: Hermann, A.J., et al., A multivariate analysis of observed and modeled biophysical variability on the Bering Sea shelf: Multidecadal.... Deep-Sea Res. II (2013), http://dx.doi.org/10.1016/j.dsr2.2013.04.007

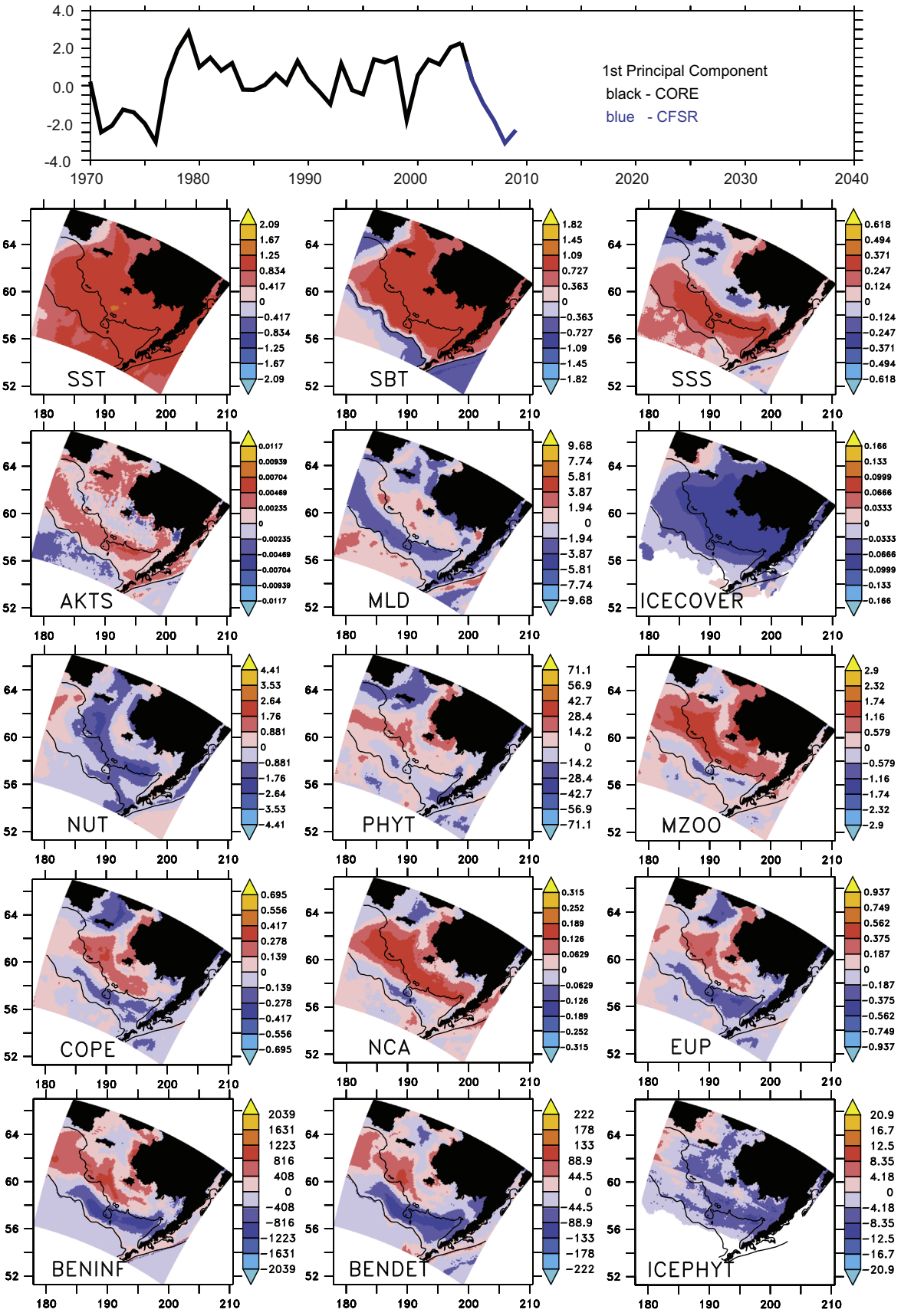

Fig. 14. Leading biophysical mode using model output from the combined CORE and CFSR hindcasts. Top figure shows the first principal component. Period of CORE (1970–2004, black line) and CFSR (2005–2009, blue line) hindcasts are indicated. This mode contains 15.1% of the total variance of the normalized timeseries. Panels exhibit the spatial loadings for each of the variables, converted back to their original units (listed in Table 3). Levels used for shading span −1 to +1 s.d. of each variable. Bathymetric contours at 70 m and 1000 m depth are shown. (For interpretation of the references to color in this figure caption, the reader is referred to the web version of this article.)

Please cite this article as: Hermann, A.J., et al., A multivariate analysis of observed and modeled biophysical variability on the Bering Sea shelf: Multidecadal.... Deep-Sea Res. II (2013), http://dx.doi.org/10.1016/j.dsr2.2013.04.007

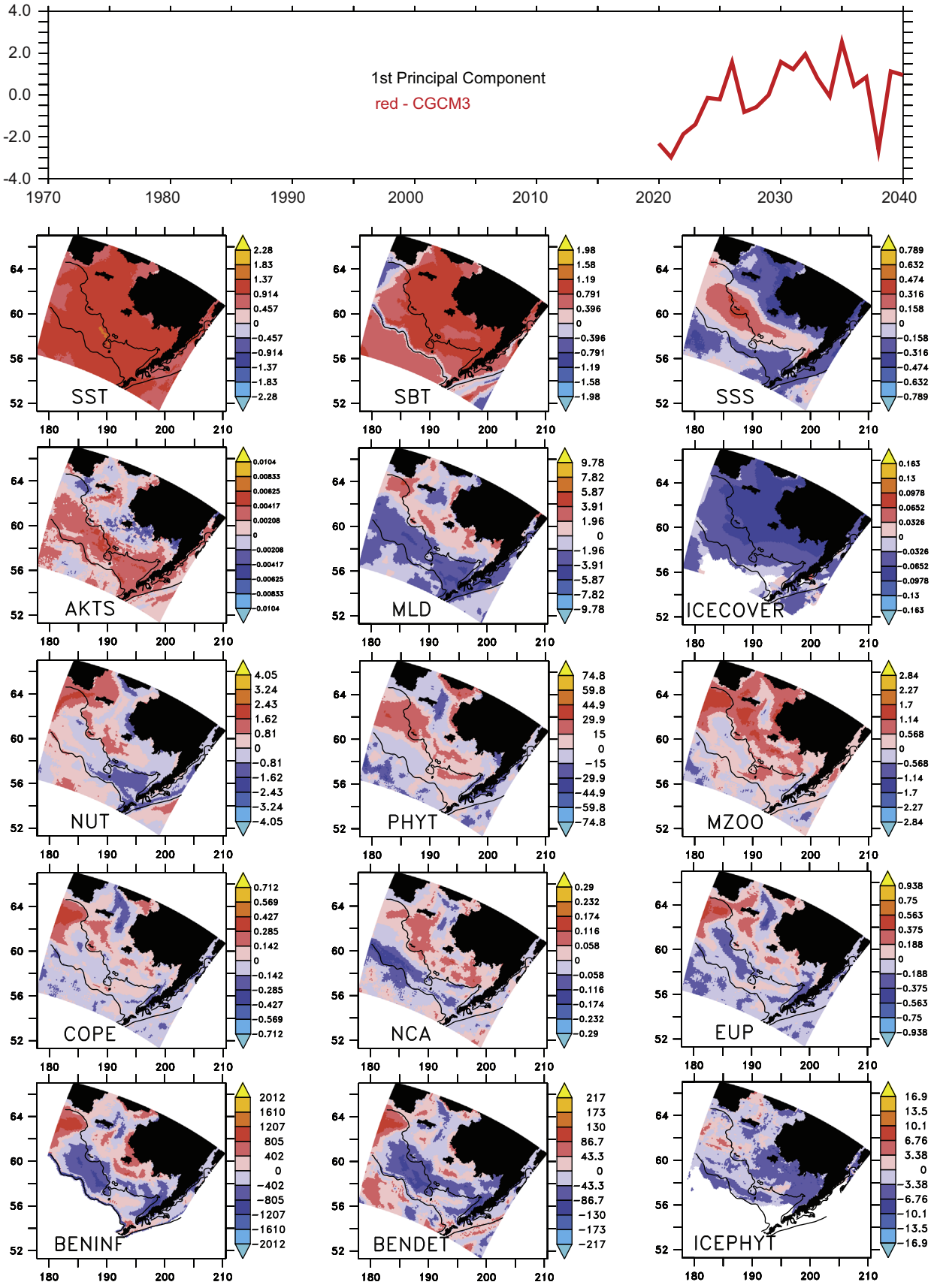

Fig. 15. Leading biophysical mode using only the last 20 years of the CGCM3 forecast (2020–2040). This mode contains 15.1% of the total variance of the normalized timeseries.

Please cite this article as: Hermann, A.J., et al., A multivariate analysis of observed and modeled biophysical variability on the Bering Sea shelf: Multidecadal.... Deep-Sea Res. II (2013), http://dx.doi.org/10.1016/j.dsr2.2013.04.007

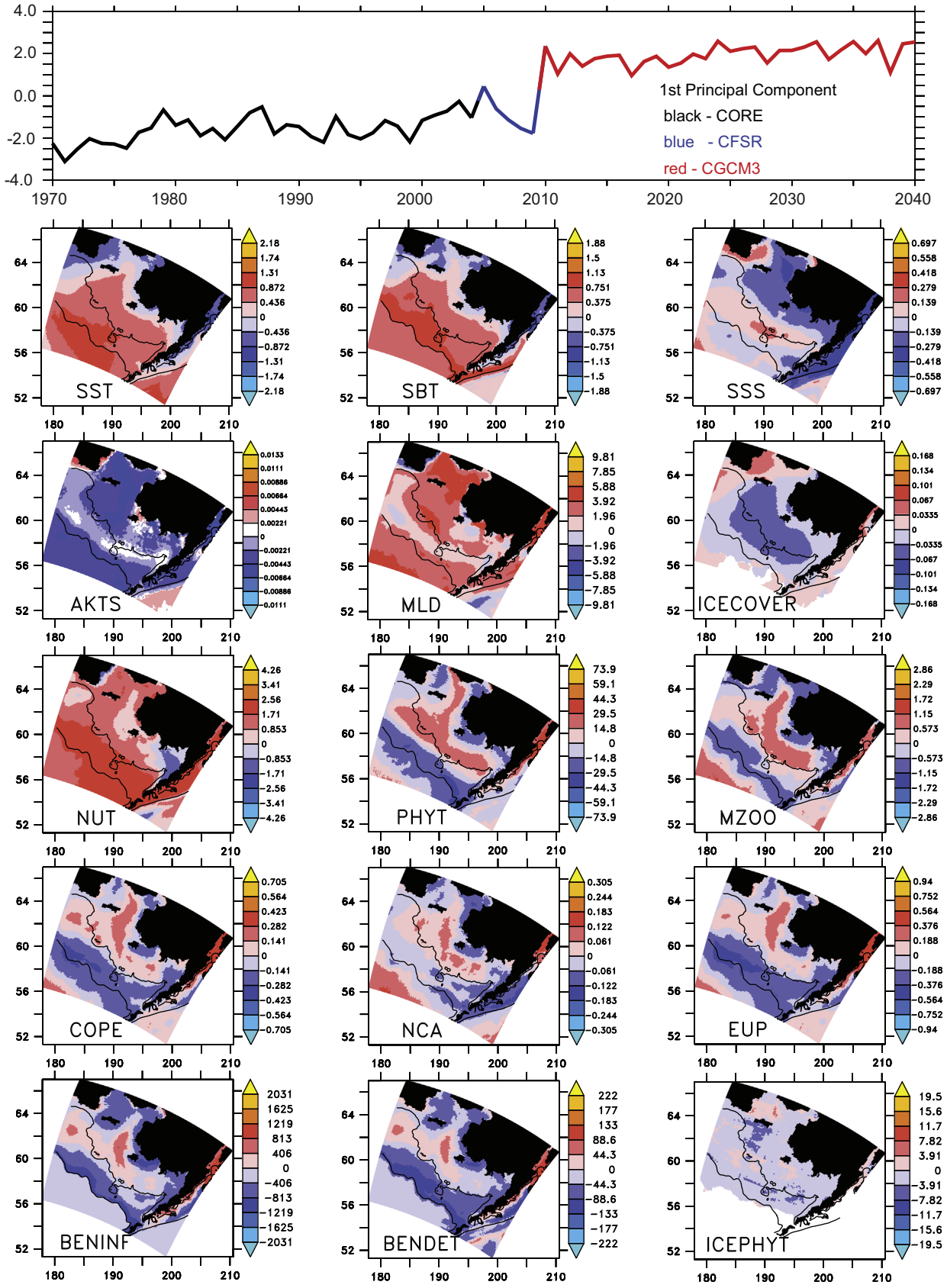

Fig. 16. Leading biophysical mode using a continuous series constructed from all three hindcasts: CORE (1970–2004, black line), CFSR (2005–2009, blue line) and CGCM3 (2010–2040, red line). This mode contains 21.5% of the total variance of the normalized timeseries. (For interpretation of the references to color in this figure caption, the reader is referred to the web version of this article.)

Please cite this article as: Hermann, A.J., et al., A multivariate analysis of observed and modeled biophysical variability on the Bering Sea shelf: Multidecadal.... Deep-Sea Res. II (2013), http://dx.doi.org/10.1016/j.dsr2.2013.04.007

ratio of growth in ice area to growth in ice thickness when freezing takes place. These will be explored in future simulations.

4.3. Differences between hindcast and forecast runs

When the full concatenated series (CORE/CFSR/CGCM3) is used in the multivariate analysis (Fig. 16), the largest jump in the PC occurs between the end of the CFSR segment and the beginning of the CGCM3 segment. The series to either side of this jump are relatively flat. This may be due in part to the mismatch between what CGCM3 predicted for the 2003–2009 period, vs. what actually occurred; as a consequence the concatenated series includes a sharp jump in temperature between 2009 and 2010 (see Fig. 9). A second source of this discontinuity may be the fact that forcing datasets in hindcast vs. forecast periods are different in spatial and temporal resolution (see Table 1). Note in particular that CGCM3 winds were only available at daily time scales, whereas CORE and CFSR were available at 6-hourly time scales. The multivariate analysis attempts to capture variance in the most efficient manner, and this first mode may in fact be composed partly of the differences between these two datasets. As an example, if there were a bias towards a more northward ice edge in CGCM3, relative to CORE or CFSR, under equivalent atmospheric conditions, the leading EOF of the combined series would contain this change in bias.

4.4. Model results vs. the oscillating control hypothesis

As summarized in Section 1.1, the modified OCH of Hunt et al. (2011) predicts that cooler temperatures will lead to a larger biomass of large crustacean zooplankton, which in turn appear necessary (albeit not sufficient) for the successful recruitment of young walleye pollock. An earlier version of the OCH (Hunt et al., 2002) suggested that warmer temperatures should lead to greater production of both small and large copepods, but this was not borne out by data from the middle and outer shelf (Hunt et al., 2011). While we cannot address the fish-related elements (and associated bottom-up vs. top-down control scenarios) of the OCH in this version of the model, we can examine the conformance of our hindcast results (Fig. 14) to the relationships among lower trophic levels in the OCH.

Specifically, the modified OCH suggests the following should occur together in the eastern Bering Sea during a warm year: warmer SST, less ice, a later bloom of phytoplankton, and a higher ratio of pelagic to benthic production. Conversely, the following should occur in a cold year: cooler SST, more ice, an earlier bloom of phytoplankton, enhanced production of large crustacean zooplankton, and a lower ratio of pelagic to benthic production. The relationships in Fig. 14 are indeed suggestive of the modified OCH, but primarily on the middle and outer shelf. Note that all the zooplankton categories are enhanced/reduced on the inner shelf

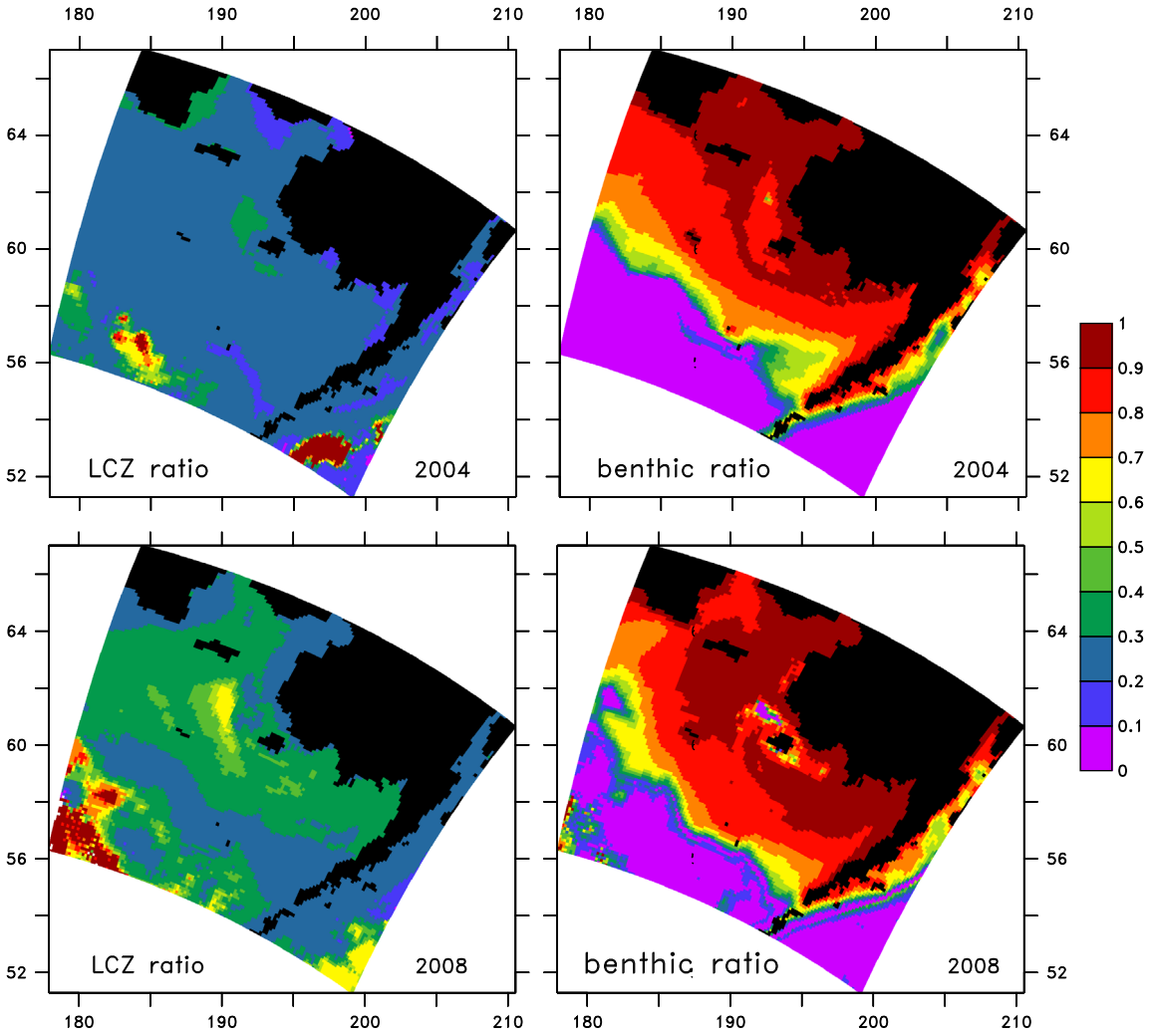

Fig. 17. Ratios of large crustacean zooplankton biomass to total zooplankton biomass (LCZ ratio), and benthic infauna biomass to total pelagic plus benthic biomass (benthic ratio), in warm (2004) vs. cold (2008) years, derived using the leading multivariate mode shown in Fig. 14.

(shoreward of the 70 m isobath) during warm/cold periods, while euphausiids and benthic biomass are significantly reduced/enhanced on the outer shelf during warm/cold periods. It would appear that for this model during 1970–2009, the inner shelf responds to higher temperatures by increasing zooplankton biomass across all size categories. By contrast, the middle and outer shelf respond to cold periods by enhancing euphausiid production (as in OCH) and enhancing benthic production (as in OCH), but only weakly enhancing small zooplankton.

A comparison of the patterns among variables in Fig. 14 suggests the following scenarios along the 70 m isobath during 1970–2009. In a cold year with more ice, lower salinity yields reduced mixing (as in Ladd and Stabeno, 2012, salinity stratification controls mixing over much of the shelf). Lower temperatures and enhanced ice cover (less light) yield lower pelagic production inshore, resulting in higher nutrient levels. Increased nutrients yield bigger zooplankton, and a shorter food chain. In a warm year, less ice results in higher salinity and enhanced mixing on the middle shelf. Higher temperatures and reduced ice cover (more light) lead to enhanced pelagic production which depletes nutrients, resulting in smaller zooplankton and a longer food chain. In each of these cases, the yearly average phytoplankton signal is modest (the timing of the bloom may shift, but that is not addressed by our analysis here).

We quantify some of these effects by reconstructing that portion of the original signal which consists of the temporal mean plus the correlated anomalies of the leading mode from the CORE/CFSR results (Fig. 14). For each variable, the anomalies are constructed by multiplying the PC timeseries by the EOF spatial patterns. Consider the case of a "warm" year (2004; PC value ~2.0) compared to a "cold year" (2008; PC value ~−3.0). The EOF values on the southern, outer shelf (195E, 65 N) are approximately +1 °C for SST, −0.25 mg C m^{-3} for MZOO and −0.25 mgC m^{-3} for EUP. In 2008, our coupled multivariate signal consists of a 3° drop in SST, accompanied by a 0.75 mg C m^{-3} increase in MZOO, a 0.75 mg C m^{-3} increase in EUP, and a 1000 mg C m^{-3} increase in BENINF.

We add these anomalies to the temporal mean at each location, and subsequently compare the ratios of large crustacean zooplankton biomass to total zooplankton biomass (LCZ ratio), and benthic infauna biomass to total pelagic plus benthic biomass (benthic ratio). For the later ratio we distribute benthic biomass (BENINF) over the depth of the water column at each location (H):

$$\text{LCZ} = \text{NCA} + \text{EUP}$$
$$\text{LCZ ratio} = \text{LCZ}/(\text{LCZ} + \text{COPE} + \text{MZOO})$$
$$\text{benthic ratio} = (\text{BENINF}/H)/(\text{LCZ} + \text{COPE} + \text{MZOO} + (\text{BENINF}/H))$$

In Fig. 17, we illustrate the results for warm (2004) vs. cold (2008) years. Both the LCZ ratio and the benthic ratio have increased in cold years. The LCZ ratio increases over the entire shelf, while the benthic ratio increases primarily on the outer, southern shelf. In this manner, the revised OCH is supported by the model all across the shelf, while an earlier version of the OCH (enhanced production of all sizes classes of zooplankton during warm periods; see Fig. 14) is supported by the model on the inner shelf alone. If COPE are included as part of the LCZ (not shown), the spatial pattern is shifted slightly, and the change in LCZ ratio is greater on the outer shelf, as compared with the version where LCZ = EUP +NCA only.

5. Conclusions

A 10-level model of the Bering Sea captures key physical and biological dynamics of the region, and has been used to explore its multiyear and multidecadal variability. Model hindcasts and forecasts have been interpreted using a form of coupled principal component analysis (CPCA). The leading mode of our CPCA analysis of biophysical model output for the Bering Sea exhibits correlated physical/biological properties with substantial interannual variability and a long-term warming trend. Several of the patterns observed conform to the revised oscillating control hypothesis (OCH). The following properties were observed:

1) All the zooplankton categories (microzooplankton, small copepods, neocalanus and euphausiids) exhibit similarities in spatial pattern, (positive correlation on the inner shelf, negative correlation on the outer shelf), but the relative magnitude of this response varies among small vs. large size classes.
2) Large crustacean zooplankton are negatively correlated with temperature on the outer, southwestern shelf, and positively correlated to temperature on the inner, northeastern shelf. Areas of positive correlation tend to correspond with those areas with greatest change in ice cover. As in the revised OCH, the ratio of large to total zooplankton is enhanced at lower temperatures. On the outer shelf, higher temperatures may be leading to reduced secondary production either through effects on stratification (and hence nutrient limitation), or through direct effects of temperature on growth, respiration, and vertical migration. Changes on the northern shelf may involve a complex interplay of light and nutrient limitation effects, as modulated by reduced ice cover. A closer examination of these relationships is warranted.
3) Salinity exhibits a strong signal at the mean location of the ice edge. As noted in Danielson et al. (2010, 2011), this likely due to the southward advection of freshwater in ice. In warm years there is less ice formation in the northeast (hence fresher there) and less ice melt at the southeastern extent of the ice (hence saltier there).
4) Benthos (benthic detritus and benthic infauna) and euphasiids are reduced on the middle and outer shelf with rising temperatures; this is correlated with a rise in both small and large zooplankton on the inner shelf. Under cold conditions, consistent with the OCH, the ratio of benthic to pelagic production appears to rise over most areas. A more explicit inclusion of production values (rather than biomass) will help to elucidate these factors.
5) Recent work by Danielson et al. (2012) underscores the importance of wind as a controlling variable which structures the Bering Sea system. In future multivariate analyses, we will utilize other groupings of variables, including the individual atmospheric forcing terms used by the model (winds and heat fluxes), to examine these relationships.

Acknowledgments

This research is contribution no. 3939 from NOAA/Pacific Marine Environmental Laboratory, and contribution ecoFOCI-0798 to NOAA's Ecosystems Fisheries Oceanography Coordinated Investigations. This publication is partially funded by the Joint Institute for the Study of the Atmosphere and Ocean (JISAO) under NOAA cooperative agreement NA10OAR4320148, contribution no. 2100. The research was generously supported by grants from the NSF sponsored Bering Sea Ecosystem Study (BEST) program (NSF-0732534), the North Pacific Research Board (NPRB) sponsored Bering Sea Integrated Ecosystem Research Program (BSIERP projects B52 and B70) and NOAA's North Pacific Climate Regimes and Ecosystem Productivity programs. This is BEST-BSIERP Bering Sea Project publication number 96 and NPRB publication number 418.

References

Allen, J.I., Somerfield, P.J., 2009. A multivariate approach to model skill assessment. J. Mar. Sys 76 (1–2), 83–94.

Andreas, E.L., Persson, P.O.G., Hare, J.E., 2008. A bulk turbulent air–sea flux algorithm for high-wind, spray conditions. J. Phys. Ocean 38, 1581–1596.

Aydin, K., Ortiz, I., Hermann, A.J. Climate to fisheries: high spatial resolution and bioenergetics in a multi-species vertically integrated model. Unpublished results.

Bretherton, C.S., Smith, C., Wallace, J.M., 1992. An intercomparison of methods for finding coupled patterns in climate data. J. Clim. 5, 541–560.

Budgell, W.P., 2005. Numerical simulation of ice-ocean variability in the Barents Sea region: towards dynamical downscaling. Ocean Dyn. 55, 370–387.

Carton, J.A., Giese, B.S., 2008. A reanalysis of ocean climate using simple ocean data assimilation (SODA). Mon. Wea. Rev. 136, 2999–3017.

Coachman, L.K., 1986. Circulation, water masses, and fluxes on the southeastern Bering Sea shelf. Cont. Shelf Res. 5 (1–2), 23–108.

Coyle, K.O., Eisner, L.B., Mueter, F.J., Pinchuk, A.I., Janout, M.A., Cieciel, K.D., Farley, E. V., Andrews, A.G., 2011. Climate change in the southeastern Bering Sea: impacts on pollock stocks and implications for the oscillating control hypothesis. Fish. Ocean 20 (2), 139–156.

Dai, A., Qian, T., Trenberth, K.E., Milliman, J.D., 2009. Changes in continental freshwater discharge from 1948–2004. J. Clim. 22, 2773–2791.

Danielson, S., Eisner, L., Weingartner, T., Aagaard, K., 2010. Thermal and haline variability over the central Bering Sea shelf: seasonal and inter-annual perspectives. Cont. Shelf Res. , http://dx.doi.org/10.1016/j.csr.2010.12.010.

Danielson, S., Curchitser, E., Hedstrom, K., Weingartner, T., Stabeno, P., 2011. On ocean and sea ice modes of variability in the Bering Sea. J. Geophys. Res. 116, C12034, http://dx.doi.org/10.1029/2011JC007389.

Danielson S., Hedstrom K., Aagaard K., Weingartner T., Curchitser E., 2012. Wind-induced reorganization of the Bering shelf circulation. Geophys. Res. Lett., 39, L08601, http://dx.doi.org/10.1029/2012GL051231.

Flato, G.M., Boer, G.J., Lee, W.G., McFarlane, N.A., Ramsden, D., Reader, M.C., Weaver, A.J., 2000. The Canadian Centre for Climate Modelling and Analysis global coupled model and its climate. Clim. Dyn. 16, 451–467.

Gibson, G.A., Hermann, A.J., Hedstrom, K. Curchitser, E.N. Response of euphausiid production to 'cold' and 'warm' years in the Bering Sea. Unpublished results.

Gibson, G.A., Spitz, Y.H., 2011. Impacts of biological parameterisation, initial conditions, and environmental forcing on parameter sensitivity and uncertainty in a marine ecosystem model for the Bering Sea. J. Mar. Syst. 88, 214–231.

Haidvogel, D.B., Arango, H., Budgell, W.P., Cornuelle, B.D., Curchitser, E., Di Lorenzo, E., Fennel, K., Geyer, W.R., Hermann, A.J., Lanerolle, L., Levin, J., McWilliams, J.C., Miller, A.J., Moore, A.M., Powell, T.M., Shchepetkin, A.F., Sherwood, C.R., Signell, R.P., Warner, J.C., Wilkin, J., 2008. Regional ocean forecasting in terrain-following coordinates: model formulation and skill assessment. J. Comput. Phys. 227, 3595–3624.

Hunt Jr., G.L., Stabeno, P., Walters, G., Sinclair, E., Brodeur, R.D., Napp, J.M., Bond, N. A., 2002. Climate change and control of the southeastern Bering Sea pelagic ecosystem. Deep-Sea Res. 49 (26), 5821–5853, http://dx.doi.org/10.1016/S0967-0645(02)00321-1.

Hunt Jr., G.L., Coyle, K.O., Eisner, L., Farley, E.V., Heintz, R., Mueter, F., Napp, J.M., Overland, J.E., Ressler, P.H., Salo, S., Stabeno, P.J., 2011. Climate impacts on eastern Bering Sea foodwebs: a synthesis of new data and an assessment of the oscillating control hypothesis. ICES J. Mar. Sci. 68 (6), 1230–1243, http://dx.doi.org/10.1093/icesjms/fsr036.

Kachel, N.B., Hunt Jr., G.L., Salo, S.A., Schumacher, J.D., Stabeno, P.J., Whitledge, T.E., 2002. Characteristics and variability of the inner front of the southeastern Bering Sea. Deep-Sea Res. II 49 (26), 5889–5909, http://dx.doi.org/10.1016/S0967-0645(02)00324-7.

Ladd, C., Bond, N.A., 2002. Evaluation of the NCEP/NCAR reanalysis in the NE Pacific and the Bering Sea. J. Geophys. Res. 107 (C10), 3158, http://dx.doi.org/10.1029/2001JC001157.

Ladd, C., Stabeno, P.J., 2012. Stratification on the Eastern Bering Sea shelf revisited. Deep-Sea Res. II 65–70, 72–83.

Large, W.G., McWilliams, J.C., Doney, S.C., 1994. Oceanic vertical mixing: a review and a model with a nonlocal boundary layer parameterization. Rev. Geophys. 32, 363–403.

Large, W.G., Yeager, S.G., 2008. The global climatology of an interannually varying air–sea 1009 flux data set. Clim. Dyn. 33, 341–364.

Marchesiello, P., McWilliams, J.C., Shchepetkin, A., 2001. Open boundary conditions for long-term integration of regional oceanic models. Ocean Model. 3, 1–20.

Preisendorfer, R.W., 1988. Principal Component Analysis in Meteorology and Oceanography. Elsevier, Amsterdam.

Saha, S., et al., 2010. The NCEP climate forecast system reanalysis. Bull. Am. Meteor. Soc. 91, 1015–1057, http://dx.doi.org/10.1175/2010BAMS3001.1.

Shchepetkin, A.F., McWilliams, J.C., 2005. The regional oceanic modeling system (ROMS): a split-explicit, free-surface, topography-following-coordinate oceanic model. Ocean Model. 9 (4), 347–404.

Simpson, J.H., Allen, C.M., Morris, N.C.G., 1978. Fronts on the continental shelf. J. Geophys. Res. 83, 4607–4614.

Stabeno, P.J., Reed, R.K., 1994. Circulation in the Bering Sea basin observed by satellite-tracked drifters: 1986–1993. J. Phys. Oceanogr. 24 (4), 848–854.

Stabeno, P.J., Bond, N.A., Kachel, N.B., Salo, S.A., Schumacher, J.D., 2001. On the temporal variability of the physical environment over the south-eastern Bering Sea. Fish. Oceanogr. 10 (1), 81–98, http://dx.doi.org/10.1046/j.1365-2419.2001.00157.x.

Stabeno, P.J., Bond, N.A., Salo, S.A., 2007. On the recent warming of the southeastern Bering Sea shelf. Deep-Sea Res. II 54 (23–26), 2599–2618, http://dx.doi.org/10.1016/j.dsr2.2007.08.023.

Stabeno, P.J., Napp, J., Mordy, C., Whitledge, T., 2010. Factors influencing physical structure and lower trophic levels of the eastern Bering Sea shelf in 2005: sea ice, tides and winds. Prog. Oceanogr. 85 (3–4), 180–196, http://dx.doi.org/10.1016/j.pocean.2010.02.010.

Stabeno, P.J., Kachel, N.B., Moore, S.E., Napp, J.M., Sigler, M., Yamaguchi, A., Zerbini, A.N., 2012. Comparis on of warm and cold years on the southeastern Bering Sea shelf and some implications for the ecosystem. Deep-Sea Res. II 65–70, 31–45.

Stabeno, P.J., Farley, E., Kachel, N., Moore, S., Mordy, C., Napp, J.M., Overland, J.E., Pinchuk, A.I., Sigler, M., 2012. A comparison of the physics of the northern and southern shelves of the eastern Bering Sea and some implications for the ecosystem. Deep-Sea Res. II, 65–70, 14–30.

Wang, M., Overland, J.E., Bond, N.A., 2010. Climate projections for selected large marine ecosystems. J. Mar. Syst. 79 (3–4), 258–266, http://dx.doi.org/10.1016/j.jmarsys.2008.11.028.

Please cite this article as: Hermann, A.J., et al., A multivariate analysis of observed and modeled biophysical variability on the Bering Sea shelf: Multidecadal.... Deep-Sea Res. II (2013), http://dx.doi.org/10.1016/j.dsr2.2013.04.007